Development of a Multisectorial Electroactive Nanowell Platform for Selective Single-Cell Sorting and Quantification

by

Lukas Menze

A thesis submitted in partial fulfillment of the requirements for the degree of

Master of Science

in

Biomedical Engineering

Department of Electrical and Computer Engineering

University of Alberta

Abstract

The rapid isolation of specific rare target cells is of rising importance in current targeted patient treatment plans. Common cell sorting approaches such as stream-based dielectrophoresis (DEP) based cell sorters are limited by their spatial dimensions as only a number of cell types corresponding to the number of output channels of the platform can be sorted. In this thesis, a microfluidic platform for selective single-cell sorting and subsequent quantification of sorted cells is presented, which can be upscaled to a high number of unique cell types without facing the same technical difficulties as previously developed devices. The platform consists of interdigitated electrodes (IDEs) and uses dielectrophoresis to capture target cells in a layer of 10 000 nanoliter wells placed on top. By splitting the design into 10 individually addressable IDE sectors, a large number of different cell types can be captured. This sectorial approach is highly modifiable and allows for complex samples to be captured over different sectors instead of requiring separate output channels for each cell type. The microfluidic behaviour of the platform regarding flow rate and DEP signal strength was examined to determine valid parameters for cell sorting and capture. A clinically relevant mixed sample of benign (MCF-10A) and malignant (MDA-MB-231) breast cells was used to validate the cell sorting performance of the platform and a target to non-target sorting accuracy of over 95% could be achieved.

To monitor sector occupancy and determine how much sample has been sorted, the capabilities of electrochemical impedance spectroscopy were ex-

amined. Experimental results revealed that impedimetric measurements can be used to quantify the number of captured cells, removing the need for an additional cell counting structure on the platform and hence reducing system complexity. Lastly, it was discussed how the presented microfluidic platform could be potentially expanded to facilitate single-cell RNA sequencing. The inability of current sequencing platforms to selectively capture and sequence cells from a mixed sample is a major problem of these designs. Since the platform presented in this thesis solves this problem, it may be a good candidate for future on-chip single-cell sequencing.

Overall, the presented microfluidic cell sorting platform shows great promise to be used as either a point-of-care device or in clinical environments where reliable sorting of varying cell samples is important.

Preface

This thesis is an original work by Lukas Menze. Credit to work not conducted by the author himself and acknowledgements were given throughout the thesis in the form of footnotes.

Some of the material presented in chapters 1, 3, and 4 has been published as L. Menze, P. A. Duarte, L. Haddon, M. Chu, and J. Chen, "Selective Single-Cell Sorting Using a Multisectorial Electroactive Nanowell Platform", DOI: 10.1021/acsnano.1c05668, `https://pubs.acs.org/articlesonrequest/AOR-NIPVNSUTZ8AWESQHFSNW`, in a forthcoming publication in *ACS Nano* and hence is reprinted with permission from the published article. Copyright 2021 American Chemical Society. I was responsible for the conceptual and actual design of the microfluidic platform, fabrication of the microfluidic platform, designing and performing experiments, data collection and analysis, as well as manuscript composition. P. A. Duarte assisted with formal analysis and device testing. L. Haddon helped with cell culture and cell staining. Both P. A. Duarte and L. Haddon contributed to manuscript edits. M. Chu supervised the biological aspects of the project and provided funding. J. Chen was the supervisory author, provided funding, and contributed to manuscript edits.

Acknowledgements

I would like to acknowledge funding provided by Mitacs. I would also of course like to acknowledge and thank Dr. Jie Chen, who gave me the freedom and resources to conduct my research. I would also like to thank Dr. Michael Chu for giving me guidance and supporting the medical and biological aspects of the project. I would like to thank Pedro Duarte for always being willing to discuss our projects and Lacey Haddon for her invaluable assistance with cell culture. Throughout the project I have worked alongside multiple research assistants, graduate students, and undergraduate students, either on my project as well as on others. To name them, in no particular order, Lian Shoute, Bingxuan Li, Zhipeng Yuan, Riley Stuermer, Nhi Ngo, and Kexin Gao. Contributions to this project done by researchers other than myself will be named and credited throughout this document.

Finally, my biggest thanks go to my parents and my brother for always being supportive of my work, and always being there when I needed them.

Contents

1 Introduction **1**
- 1.1 Thesis goals . . . 2
- 1.2 Thesis outline . . . 3

2 Theory **5**
- 2.1 Cell sorting . . . 5
  - 2.1.1 Fluorescence activated cell sorting . . . 5
  - 2.1.2 Magnetic activated cell sorting . . . 6
- 2.2 Dielectrophoresis . . . 7
  - 2.2.1 Fundamentals of dielectrophoretic particle manipulation 7
  - 2.2.2 The n-shell model . . . 8
  - 2.2.3 Clausius-Mossotti factor . . . 9
  - 2.2.4 Dielectrophoresis activated cell sorters . . . 12
  - 2.2.5 Cell sorting using electroactive nanowells . . . 14
- 2.3 Electrochemical impedance spectroscopy . . . 14
  - 2.3.1 Modelling of coplanar electrodes . . . 15

3 Materials and Methods **18**
- 3.1 Microfluidic platform . . . 18
  - 3.1.1 Chip fabrication . . . 18
  - 3.1.2 Assembly . . . 21
- 3.2 Cell preparation . . . 23
  - 3.2.1 Cell culture . . . 23
  - 3.2.2 Cell staining . . . 23
  - 3.2.3 DEP buffer preparation . . . 24
- 3.3 Experimental setup . . . 24
  - 3.3.1 Chip-holder . . . 24
  - 3.3.2 External equipment . . . 26

4 Development of cell sorting platform **27**
- 4.1 Proof-of-concept experiments and designs . . . 27
  - 4.1.1 First iteration of the microfluidic platform . . . 27
  - 4.1.2 Preliminary results and discussion . . . 27
- 4.2 Development of multisectorial platform . . . 30
  - 4.2.1 Design and operating principle . . . 30

4.2.2 Dielectrophoresis-assisted cell capture 32
4.2.3 Dielectrophoresis-assisted cell sorting 39
4.3 Conclusion 45

5 Cell quantification **46**
5.1 Configuration of platform 46
5.1.1 Impedimetric quantification of sector occupancy 46
5.1.2 Discussion 50
5.2 Improved chip-holder 51
5.2.1 Design choices and operating principle 51
5.3 Conclusion 53

6 Ongoing and future work **54**
6.1 Expansion to single-cell RNA sequencing platform 54
6.1.1 Modified platform design 55
6.1.2 Single-cell RNA sequencing process flow 56
6.2 Integrated point-of-care device 57
6.3 Conclusion 60

7 Conclusion **61**

References **63**

Appendix A Particle parameters **72**

Appendix B Mask designs **74**

Appendix C PCB design **78**

List of Tables

2.1 Dielectric parameters of HEK-293 cells, yeast cells, and polystyrene beads 10

4.1 Dielectric parameters of MDA-MB-231 and MCF-10A cells . . 40

A.1 Detailed parameters of polystyrene bead 72
A.2 Detailed parameters of HEK-293T, MDA-MB-231, and MCF-10A cells 72
A.3 Detailed parameters of yeast cell 73

List of Figures

2.1 Fluorescence activated cell sorting 6
2.2 Dielectrophoresis facilitated particle movement 8
2.3 n-shell models 9
2.4 CM curves for HEK-293 cells, yeast cells, and polystyrene beads 11
2.5 Stream-based dielectrophoresis assisted cell sorter 12
2.6 Dielectrophoresis activated cell sorting using field-flow fractionation 13
2.7 Cell sorting using electroactive nanowells 15
2.8 Equivalent circuit model for two coplanar electrodes 16
2.9 Magnitude and phase frequency responses of the impedance for a coplanar electrode system 17
2.10 Equivalent circuit model for two coplanar electrodes including passing cells 17

3.1 Microfluidic chip fabrication process flow 20
3.2 APTES bonding process 22
3.3 Chip-holder iterations 25
3.4 Experimental setup 26

4.1 Proof-of-concept design 28
4.2 Problems encountered with proof-of-concept design 29
4.3 Assembled microfluidic platform 31
4.4 Nanowell structure of microfluidic platform 31
4.5 Operating modes of microfluidic platform 32
4.6 Sector occupancies obtained at different flow rates and a fixed DEP signal amplitude of 15 V_{pp} 34
4.7 Sector occupancies obtained at different DEP signal amplitudes and a fixed flow rate of 0.8 μL/min 36
4.8 COMSOL Multiphysics simulations of channel height 38
4.9 Fluorescent images of captured MDA-MB-231 cells at different settings 39
4.10 Schematic representation of experiments evaluating the cell sorting performance of the platform 41
4.11 Real part of the CM factor for both MDA-MB-231 and MCF-10A cells 42

4.12 Fluorescence images of cell sorting 43
4.13 Cell sorting performance for different sector and frequency configurations with the same signal applied to both sectors 44
4.14 Cell sorting performance for different sector and frequency configurations with a different signal applied to both sectors . . . 44

5.1 Measured impedance frequency responses obtained for different sector occupancies 48
5.2 Calibration curves of the normalized impedance magnitude and phase 50
5.3 Block diagram of modified chip-holder design 52
5.4 Interleaved application of DEP and EIS signals to a sector . . 52

6.1 Double-well design of scRNA-Seq modification 56
6.2 Capture of RNA primer coated beads 56
6.3 Process flow of single-cell RNA sequencing on modified platform 58
6.4 Block diagram of integrated point-of-care device 59

B.1 Mask design used for proof-of-concept experiments 74
B.2 Mask design of the microfluidic platform 75
B.3 Mask design used to study RNA coated polystyrene beads . . 76
B.4 Mask design used for single-cell RNA sequencing 77

C.1 PCB layout of modified chip-holder 78
C.2 PCB schematic of modified chip-holder 79

Glossary

APTES (3-Aminopropyl)triethoxysilane

CM Clausius-Mossotti

CTC Circulating Tumor Cell

DACS Dielectrophoresis Activated Cell Sorting

DEP Dielectrophoresis

EIS Electrochemical Impedance Spectroscopy

FACS Fluorescence Activated Cell Sorting

FFC Flat Flex Cables

FFF Field-flow fractionation

IDE Interdigitated Electrode

IPA Isopropyl Alcohol

MACS Magnetic Activated Cell Sorting

nDEP Negative Dielectrophoresis

nF-EIS Non-Faradaic Electrochemical Impedance Spectroscopy

PCB Printed Circuit Board

pDEP Positive Dielectrophoresis

PDMS Polydimethylsiloxane

POC Point-of-Care

PTFE Polytetrafluoroethylene

RNA Ribonucleic Acid

scRNA-Seq Single-cell RNA Sequencing

Chapter 1

Introduction

With the advances in targeted cancer therapy over the last decade, there has been a growing need for a portable and low-cost platform that can rapidly and reliably sort complex heterogenous cell mixtures. This is especially important in autologous patient treatments, where it is crucial to sort through a large sample in order to selectively detect and single out a rare target species, such as hematopoietic stem cells (HCTs) or circulating tumor cells (CTCs).[1]–[4] Furthermore, such a platform could serve as a research platform for the identification of novel cell populations within a tumor microenvironment, a critical factor in tumor progression. The genomic and transcriptomic profiles of these unique populations may offer insights into tumor resistance and identify important therapeutic targets in a variety of cancers.[5] Single-cell sorting is of increasing importance in precision medicine applications such as advanced genomics or next-generation sequencing.[6]–[8] State-of-the-art systems for cancer detection, such as CellSearch,[9], [10] OncoDiscover,[11] or CellMax,[12], [13] capture and isolate CTCs from patient samples. Subsequent quantification of the number of CTCs then may provide important information about the state of a patient. In single-cell RNA sequencing platforms, such as in the commercially available 10x Genomics solutions [14], [15] or recent advances,[16]–[18] it is crucial to ensure that only the target cells are sequenced for accurate results. Hence, depending on the mechanism of the sequencing platform, reliable cell sorting prior to loading the sequencing platform may be required.

Traditionally used cell sorting approaches include density gradient-based methods as well as fluorescence activated cell sorting (FACS) and magnetic activated cell sorting (MACS). In both FACS and MACS, the sample has to be prepared and correctly labelled with either fluorescent stains or magnetic microbeads in order to be sorted successfully.[1], [4] Dielectrophoresis activated cell sorting (DACS) offers an alternative approach based on the intrinsic characteristics of dielectrophoresis (DEP) to sort cells without the need for any prior labelling. DEP is an electrokinetic phenomenon that allows for the selective manipulation of dielectric particles, such as mammalian cells, via polarization when subjected to a spatially non-uniform electric field.[19], [20] Reported microfluidic DACS structures mainly focus on sorting cells by positioning electrodes in a microfluidic channel and subsequently use DEP to change the flow trajectory of passing cells depending on their dielectric characteristics, hence directing them into different output channels.[21]–[26] These designs are innately limited by the number of output channels, as the number of individually sorted cell types directly corresponds to the number of outlets. Other less common DEP-based cell sorting approaches employ field-flow fractionation to sort different cell types.[27]–[30] Another limitation these designs face is their inability to readily provide information about the number of sorted cells. Additional cell counting structures such as microfluidic Coulter counters, which have been shown to reliably detect single cells,[31]–[33] may be employed to count the number of cells flowing through an outlet channel, at the cost of an increased overall system complexity. Therefore, an integrated platform that allows for simple and accurate monitoring of the number of sorted cells would be desirable.

1.1 Thesis goals

In this thesis, a microfluidic platform that uses a nanowell structure in combination with interdigitated electrodes (IDEs) to sort and capture single cells is presented. Micro- and nanowell arrays have already been extensively used for various biomedical applications, such as malignant cell identification and

characterization,[18], [34]–[36] cell pairing and molecular interaction,[37]–[39] and cell sequencing.[16], [17], [40], [41] Commonly, these devices feature thousands of microwells that are subsequently analyzed by imaging and microscopy. While microwell loading traditionally occurred via gravity,[16], [42]–[44] active trapping mechanisms such as DEP have been used lately to improve the capture efficiency.[17], [18], [34], [45]–[47] Recent advances that combine microwells with DEP range from devices featuring 300 000 microwells used for the molecular analysis of tumor cells [18] to devices achieving double-sub-Poisson single-cell RNA sequencing with 3600 nanowells.[17]

The main goal of the developed microfluidic platform is to reliably sort cells with a high accuracy. In contrast to already reported DACS systems, the emphasis of the platform is on reducing system complexity rather than aiming at high-throughput sorting. The platform should be readily usable with various samples or easily modifiable to do so. Ideally, it should also allow for the simultaneous sorting of a number of different cell types, hence bypassing the cell type to channel outlet restriction posed by other cell sorters.

Another major goal is to use the IDEs employed for DEP capture for accurate monitoring of captured cells. Achieving this would reduce system complexity and would provide information of how much sample has been sorted. This thesis explores the capabilities of electrochemical impedance spectroscopy, a label-less measurement technique, to accomplish this.

1.2 Thesis outline

This thesis is organized to show the design process of the microfluidic platform, beginning with the theoretical aspects required and ending with future and ongoing work. In chapter 2, the main concepts required for dielectrophoretic cell sorting and impedimetric cell detection are introduced. Chapter 3 covers the platform fabrication and assembly as well as details regarding cultured cells and buffer solutions used. Chapter 4 focuses on the platform development, from early proof-of-concept to the final platform design. Emphasis is on the DEP assisted cell capture as well as cell sorting performance of the final design.

Chapter 5 then discusses the cell detection and quantification capabilities of the platform achieved with electrochemical impedance spectroscopy. Chapter 6 outlines ongoing and future work, including how the platform can be modified to a single-cell RNA sequencing device as well as an overview of what components are needed to integrate the platform into a stand-alone point-of-care device. Finally, chapter 7 ends the thesis with an overarching conclusion, detailing how the original thesis goals have been fulfilled and how the initial design has evolved into a platform not only limited to cell sorting but also expandable to single-cell sequencing.

Chapter 2

Theory

2.1 Cell sorting

Cell sorting describes the process of separating a number of different cell types in a heterogeneous sample. An example of this would be the separation of a certain type of cell, such as red blood cells, from a blood sample. Nowadays, cell sorting is of growing importance in patient-specific treatment plans, such as in targeted cancer treatments.[1]–[4] Over the years, a multitude of different cell sorting approaches have been developed, each having their own advantages and disadvantages.

2.1.1 Fluorescence activated cell sorting

Fluorescence activated cell sorting (FACS) is the classical approach to cell sorting ever since the first commercial FACS device was invented by Herzenberg *et. al* in 1969.[48] FACS applies fluorescent labels to cell populations to enable cell type identification. Labelled populations are introduced into a microfluidic channel and subsequently pass a focused laser beam that facilitates inspection and identification of the current passing cell (Figure 2.1).[1], [4] Depending on the detected cell type, the cell is then discretely sorted into one of the outlet channels via various possible mechanisms, such as electrokinetic mechanisms,[49]–[51] acoustophoresis,[52]–[54] or optical manipulation.[55]–[57] Nowadays, FACS is the most common cell sorting technique used due to its reliability, ease of use, and high efficiency.[1], [4], [49]

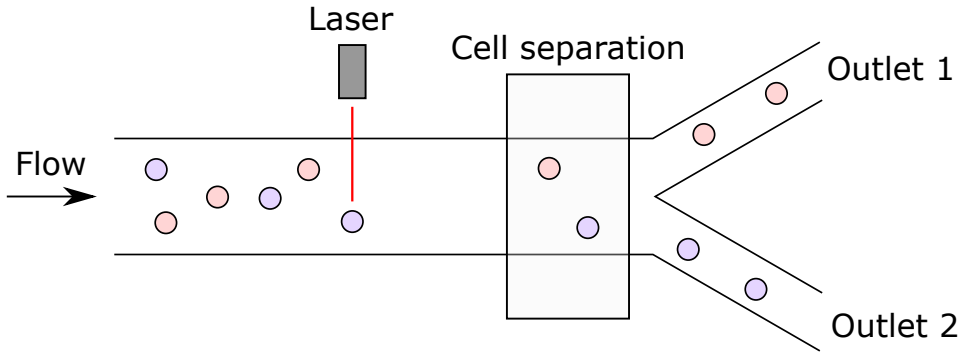

Figure 2.1: Schematic representation of fluorescence activated cell sorting. Cell populations tagged with fluorescence labels are identified by a focused laser and subsequently separated into different outlet channels via various separation techniques, such as electrokinetics or acoustophoresis.

2.1.2 Magnetic activated cell sorting

In magnetic activated cell sorting (MACS), cells are magnetically labelled with ferromagnetic nanoparticles. Cell populations are subsequently sorted when they pass a magnetic field gradient as the exerted magnetic force depends on the amount of nanoparticles on a cell.[1], [4] Hence, larger cells are subject to a greater magnetic force. MACS is particularly attractive for separating otherwise sparse cell populations, such as circulating tumour cells (CTCs). CTCs and other rare cells can be specifically labelled with antibodies containing ferromagnetic nanoparticles and then reliably sorted from the bulk sample.[58]–[60]

Both FACS and MACS require preparation and label application to successfully sort cell populations. Hence, in areas requiring rapid sorting of various and changing cell types label-free sorting mechanisms are desired. Dielectrophoresis can be employed to provide such a solution as it enables populations to be sorted based on their intrinsic dielectric parameters.

2.2 Dielectrophoresis

2.2.1 Fundamentals of dielectrophoretic particle manipulation

Since the detailed studies on dielectrophoresis (DEP) and its effects on particles done by Herbert Pohl in the 1950s and 1960s, DEP has gained a lot of attention in biomedical and lab-on-chip systems. Its innate characteristics allow DEP to be a highly selective and label free technique for particle manipulation.[19], [20], [61] When an electrically polarizable particle such as a cell enters a non-uniform electric field, it will become subject to a DEP force F_{DEP} that arises from the interaction between the electric field and the thereby induced dipole of the particle. Depending on whether the particle is attracted towards regions exhibiting the maximum electric field gradient, such as the electrode edges, or expelled from them, F_{DEP} is defined as positive (pDEP) or negative (nDEP), respectively (as shown schematically in Figure 2.2).[33], [34] F_{DEP} acting on a given particle with radius r is expressed by

$$F_{DEP} = 2\pi r^3 \varepsilon_m \mathrm{Re}\left\{\mathrm{CM}\right\} \nabla \left|E_{rms}\right|^2 \tag{2.1}$$

where ε_m is the conductivity of the medium in which the particle is suspended and E the applied electric field. The bracketed expression is the real part of the Clausius-Mossotti (CM) factor and determines whether the particle experiences a positive or negative DEP force. The CM factor describes the dielectric relationship between particle and suspension medium and hence varies greatly between different particle types and suspension media. Since biological samples such as cells or fungal spores are more complex and feature more individual components when compared to solid particles, i.e. polystyrene beads, mathematical models that aim to combine the different components have to be used to obtain an accurate estimate of the CM factor. Note that F_{DEP} depends on the electric field, as well as the polarization of the particle, the latter being proportional to the polarizing field for linear dielectric particles, thus causing a square dependence. This is similar to the force exerted by optical tweezers. [62]

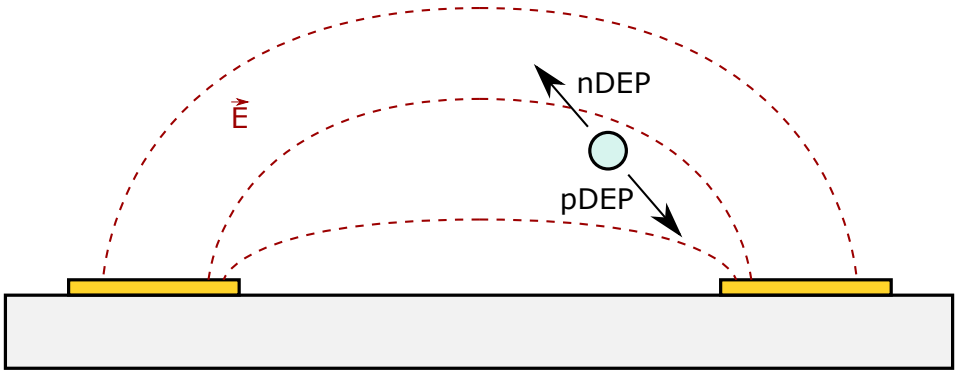

Figure 2.2: Particle movement due to DEP. The electric field is being applied via two coplanar electrodes. pDEP forces the particle to move to regions showing a higher field gradient. Similarly, nDEP forces the particle towards regions with a lower field gradient.

2.2.2 The n-shell model

Most commonly, the n-shell, or multi-shell, model is used to model the dielectric parameters of biological particles. A single shell consists of two layers, the shell surface (outer layer) and the contents within the shell (inner layer), as shown in Figure 2.3a. In a cell, these two layers may represent the cytoplasm surrounded by the cell membrane. The onion-like structure of the model allows for easy inclusion of additional individual components by expanding the model with additional layers.[63]–[65] Most mammalian cells can be modelled sufficiently well with a double-shell model (Figure 2.3b). The mathematical expression for the combined complex permittivity ε^*_{comb} of two layers with radii r_1 and r_2 is

$$\varepsilon^*_{comb} = \varepsilon^*_2 \frac{\left(\frac{r_2}{r_1}\right)^3 + 2\left(\frac{\varepsilon^*_1 - \varepsilon^*_2}{\varepsilon^*_1 + 2\varepsilon^*_2}\right)}{\left(\frac{r_2}{r_1}\right)^3 - \left(\frac{\varepsilon^*_1 - \varepsilon^*_2}{\varepsilon^*_1 + 2\varepsilon^*_2}\right)} \tag{2.2}$$

where the indices 1 and 2 denote the inner and outer layer, respectively. The complex permittivity ε^* is given by

$$\varepsilon^* = \varepsilon + j\frac{\sigma}{\omega} \tag{2.3}$$

where ε is the real part of the permittivity, σ the conductivity, $j = \sqrt{-1}$, and ω the angular frequency of the applied electric field.

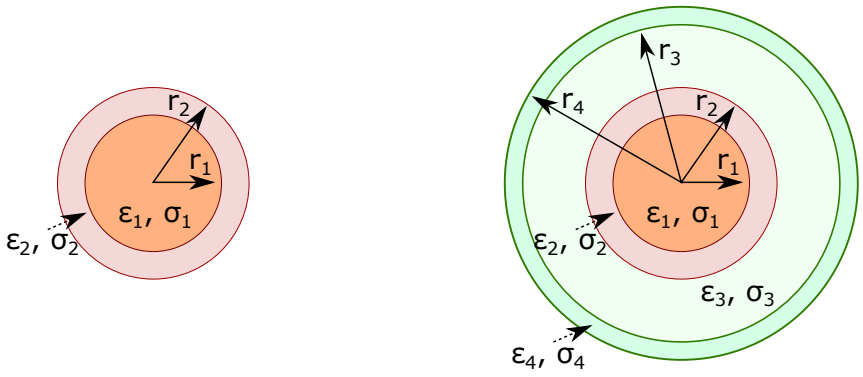

(a) Single-shell model. (b) Double-shell model.

Figure 2.3: n-shell models. Figure 2.3a shows a single-shell model, while Figure 2.3b shows a double-shell model. Each shell consists of an inner and outer layer.

2.2.3 Clausius-Mossotti factor

In mammalian cells, the dielectric properties are generally closely tied to the physiological cell characteristics such as cytoplasm conductivity or membrane capacitance.[66]–[69] Additionally, there is a significant difference in cell properties between healthy and malignant cells.[27], [70], [71] To understand the DEP response of different cell types in different buffers, the Clausius-Mossotti (CM) factor has to be calculated. The CM factor effectively describes the frequency-dependent relationship between the dielectric parameters of a particle and its suspension medium [33], [34] and is expressed by

$$\mathrm{CM} = \frac{\varepsilon_p^* - \varepsilon_m^*}{\varepsilon_p^* + 2\varepsilon_m^*} \tag{2.4}$$

The indices p and m denote the complex permittivity for particle and medium, respectively. If the real part of the CM factor is positive, the particle experiences pDEP and is attracted towards regions of maximum field gradient. Consequently, if the real part of the CM factor is negative, the particle will move towards regions of minimum electric field gradient. DEP capture refers to the movement of particles towards the electrodes as they exhibit the maximum field gradient, where they will become trapped either on the electrode itself or in structures manufactured on top of the electrodes, commonly referred to as

DEP traps.

To obtain the CM factor for cells, the previously introduced n-shell model has to be used. Table 2.1 gives reported dielectric parameter values for yeast and HEK-293 cells in addition to values for an arbitrary polystyrene particle. From these values, it is evident that the dielectric parameters between the two cell types as well as of their individual components are quite different. More details such as layer radii can be found in Appendix A. Figure 2.4 shows the calculated CM factor curves of those three particles suspended in a buffer with a permittivity of $80\varepsilon_0$ and conductivity of 0.02 S/m.

Parameter	HEK-293 cell	Yeast cell	Polystyrene bead
$\varepsilon_{r,cytoplasm}$	60	50	
$\sigma_{cytoplasm}$ (S/m)	0.5	0.2	
$\varepsilon_{r,membrane}$	9.5	6	
$\sigma_{membrane}$ (S/m)	$7 * 10^{-14}$	$25 * 10^{-8}$	
$\varepsilon_{r,wall}$		60	
σ_{wall}(S/m)		$14 * 10^{-3}$	
$\varepsilon_{r,bead}$			2.6
σ_{bead}(S/m)			$5 * 10^{-4}$

Table 2.1: Dielectric parameters of HEK-293 cells,[72] yeast cells,[73] and arbitrary polystyrene beads.

Whereas both HEK-293 and yeast cells experience pDEP for certain frequencies, the chosen polystyrene beads only experience nDEP. Hence, HEK-293 cells can be attracted and trapped for frequencies between 3 kHz and 6 MHz, as this is where the CM curve shows positive values. For yeast cells, this regime is slightly smaller and ranges from 9 kHz to approximately 4 MHz. As seen in Equation 2.1, a higher CM value correlates to a higher DEP force, indicating that for optimal particle manipulation the frequency of the applied electric field should be chosen in such a way that the CM value is maximized. Additionally, cell separation between two types of cells can be facilitated when at a given frequency one of them experiences nDEP or no substantial DEP while the other experiences pDEP and is attracted towards the electrodes. Hence, using DEP to sort cells provides for a highly selective and label-free method of cell sorting.

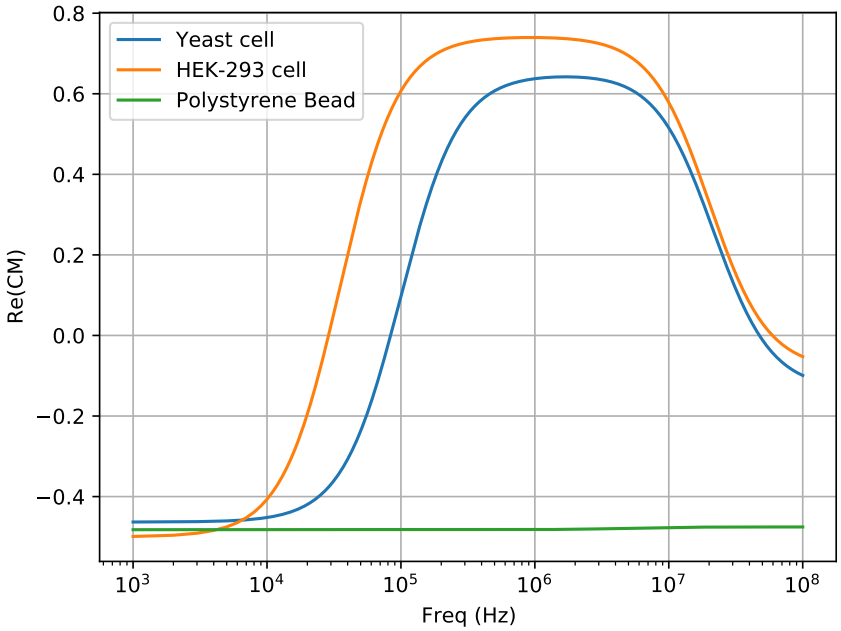

Figure 2.4: Plotted CM curves of HEK-293 cells, yeast cells, and polystyrene beads. Whereas in this particular buffer both HEK-293 and yeast cells can experience both positive or negative DEP, depending on the applied frequency, polystyrene beads only experience negative DEP. Consequently, DEP capture of these type of beads would not be possible with this buffer.

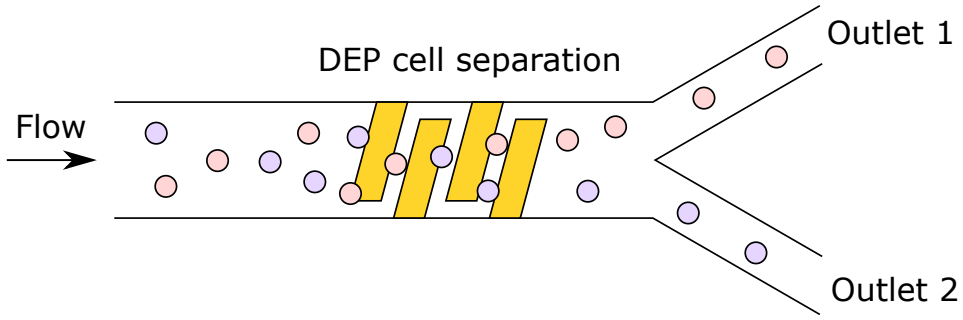

Figure 2.5: Dielectrophoresis activated cell sorting in a stream-based cell sorter. The electrodes are placed at a certain angle towards the flow direction, changing the trajectory of cells depending on their dielectric properties. The applied DEP signal has to be chosen in such a way to ensure that each cell population enters its individual outlet channel.

2.2.4 Dielectrophoresis activated cell sorters

Currently used dielectrophoresis activated cell sorters (DACS) can be divided into two major subcategories. Stream-based cell sorters sort particles by using DEP to change their respective trajectories (Figure 2.5) and are the most common form of DACS. Cells with different trajectories are then flowed into different outlet channels. While this method has a high sorting throughput, the number of different cell populations that can be successfully sorted at a given time are limited by the number of outlets. Increasing the number of outlets increases the overall system complexity in addition to dimensional parameters such as channel length and width, which would have to be enlarged to maintain successful sorting capabilities.[21]–[26]

The second and less common method employs field-flow fractionation (FFF) to sort cell types depending on their relative speed to each other. As particles following the pressure-driven flow profile exhibit the lowest speed among the channel walls and the highest in the middle of the channel, cells that are affected by gravity and subsequently move towards the bottom of the chip hence move slower and take a longer time to exit the channel. nDEP is used to let cells float at a certain channel height, thus controlling their relative speed. Figure 2.6 shows schematically how this spatial separation is achieved. While this approach only needs one outlet channel, potential problems may arise when cells that were supposed to flow in the middle of the channel in-

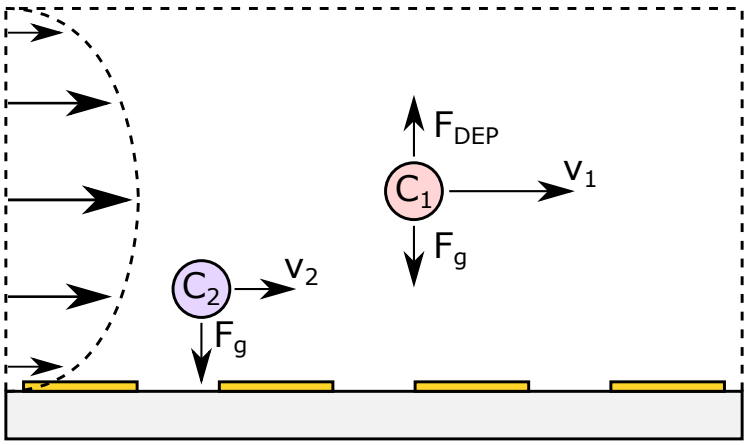

Figure 2.6: Dielectrophoresis activated cell sorting using field-flow fractionation. The red cell C_1 flows in the middle of the channel as DEP pushes it upwards and hence has the maximum velocity v_1. DEP is tuned in a way that an equilibrium is reached between F_{DEP} and the gravitational force F_g. Additionally, the purple cell C_2 experiences no substantial DEP force for this example. Subsequently, C_2 flows near the bottom of the channel and has a lower velocity v_2.

stead flow near the channel walls as a consequence of external other factors, such as an incorrect tuning between F_{DEP} and gravitational pull or unwanted turbulences. This would lead to an incomplete separation of the mixed populations. Additionally, the length of FFF sorting chip has to be considered. As the spatial separation of cell populations depends on the difference of flow speed, a certain channel length is required to successfully separate the given populations.[27]–[30]

While both approaches can be used to accurately and rapidly sort large cell populations, they also have their own respective drawbacks. DACS based on individual nanowells offers an alternative that trades high throughput against a modular and multisectorial design and the ability to sort a great number of different populations at the same time. Additionally, the nanowell platform offers the possibility to be used for future single-cell operations, such as single-cell RNA sequencing. Note that in all DEP platform approaches particles flowing near the channel walls may get charged by rubbing against the channel wall and hence may behave differently when entering the applied electric field.

2.2.5 Cell sorting using electroactive nanowells

The nanowell platform features a multisectorial design consisting of multiple electrode structures. Each sector contains a minimum of two individually addressable electrodes. Nanowells designed to only hold a single captured cell are placed on top of the electrodes to facilitate DEP capture. In contrast to the previously introduced DACS, this approach aims at first capturing cell populations and releasing them later on, instead of achieving an in-line high-throughput. The simplest case for nanowell assisted cell sorting would be sorting of two populations. In this case, one population would be trapped in the nanowells while the other population would not be affected by DEP and hence continue to exit the channel.

Since each sector can be addressed independently, each sector can capture a different cell population, as shown in Figure 2.7. This also facilitates more complex multi-stage sorting designs, where the gradual sorting of certain cell types is important, i.e. prefiltering of a "dirty" sample. The modular sector approach allows for easy expansion either by enlarging a given sector or by adding new ones. Depending on the size of sorted cells however, the nanowell height and diameter may need to be adjusted to ensure single-cell capture.

Another benefit of the nanowell design is the ability to use the electrodes for both DEP capture and in-line detection of sorted cells. Electrochemical impedance spectroscopy (EIS) measurements provide information about the number of captured cells and hence the amount of the sample that still needs to be sorted. In other DACS, this is done with additional cell counting structures, such as Coulter counters, which have been shown to reliably detect single cells.[31]–[33] However, each additional structure increases the overall system complexity, hence the need for integrated solutions.

2.3 Electrochemical impedance spectroscopy

Electrochemical impedance spectroscopy (EIS) can be used to monitor the change in impedance between a pair of electrodes, which naturally occurs when a particle passes over them. EIS is classified into two distinct techniques,

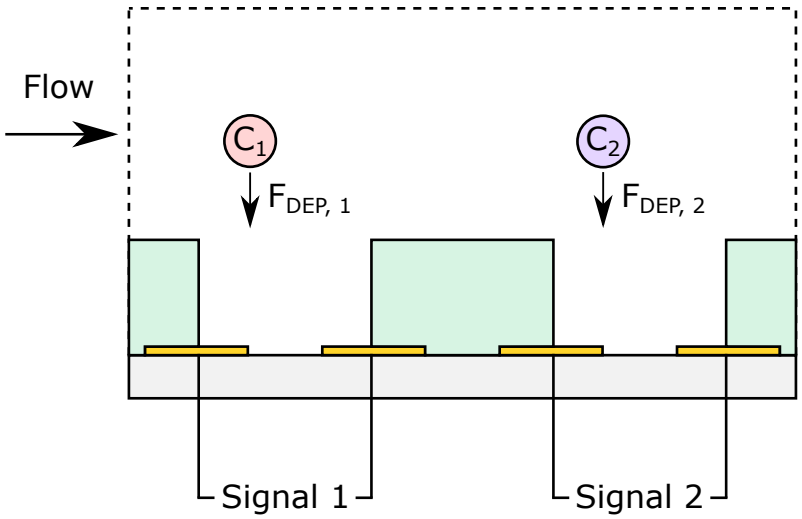

Figure 2.7: Schematic view of nanowell assisted cell sorting. Cells are attracted by pDEP and trapped in individual nanowells. The sectorial design allows different sectors of the chip to be addressed individually and hence enables the capture of multiple cell populations on one microfluidic chip. In the chip section example shown here signal 1 only facilitates DEP capture of cell type 1 whereas signal 2 is used to selectively capture cell type 2.

faradaic and non-faradaic EIS. Faradaic EIS is more sensitive to impedance changes but in turn requires a more complex electrode setup with the need for an additional reference electrode and specific electrochemical reactions.[74]–[77] In contrast, non-faradaic EIS does not depend on electrochemical reactions as changes of the electrical system properties caused by the interaction with biomolecules, such as particles, are measured. To achieve this, small signals are applied to the electrodes and the current response is recorded.[78]–[80]

2.3.1 Modelling of coplanar electrodes

The electrode structure that is most commonly used for DEP capture or counting structures, i.e. Coulter counter, is a set of coplanar electrodes. The platform developed in this thesis also features coplanar electrodes. Figure 2.8 shows the equivalent circuit model for a basic two-electrode system, aiming at representing the geometrical properties of the electrodes as well as the characteristics of the surrounding buffer solution. The capacitance C_g represents the geometric capacitance of the electrode structure itself and hence is subject to the electrode dimensions, such as length and gap between them, as well as the

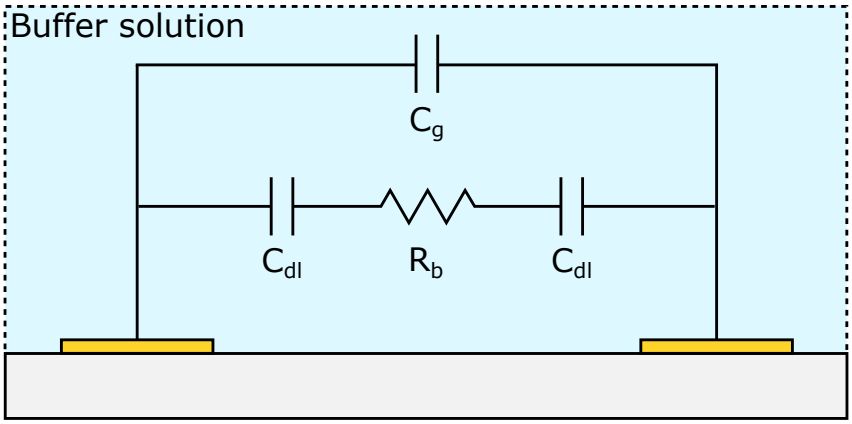

Figure 2.8: Equivalent circuit model for two coplanar electrodes surrounded by a buffer solution.

dielectric properties of the buffer around it. The double layer capacitances C_{dl} represent the interaction between charged ions in the buffer and the electrode surface charge. Lastly, the resistance of the buffer is included by the resistor element R_b.[80], [81] From this follows the overall system impedance

$$Z_{sys} = \left(R_b + \frac{2}{j\omega C_{dl}} \right) \parallel \frac{1}{j\omega C_g} \tag{2.5}$$

where $j = \sqrt{-1}$ and ω is the angular frequency. More complex circuit models have also been reported, however, they include effects that generally do not have to be considered in non-faradaic EIS.[82], [83]

Plotting Equation 2.5 gives the typical frequency response curves shown in Figure 2.9. The frequency responses for both magnitude and phase show three distinct regions. In the first region, up until cutoff frequency f_L, the impedance decreases steadily while the phase stays at larger values and Z_{sys} is dominated by the double layer capacitance. Subsequently, between cutoff frequencies f_L and f_H the system is dominated by R_b and hence becomes resistive, leading to a decrease in phase while the magnitude stays constant with increasing frequency. In the last region, for frequencies greater than f_H, the system becomes capacitive again as seen by the large phase value and magnitude decrease with increasing frequency. This region is dominated by the geometric capacitance. [80], [81]

If a cell passes over the electrodes, the equivalent circuit model needs to be

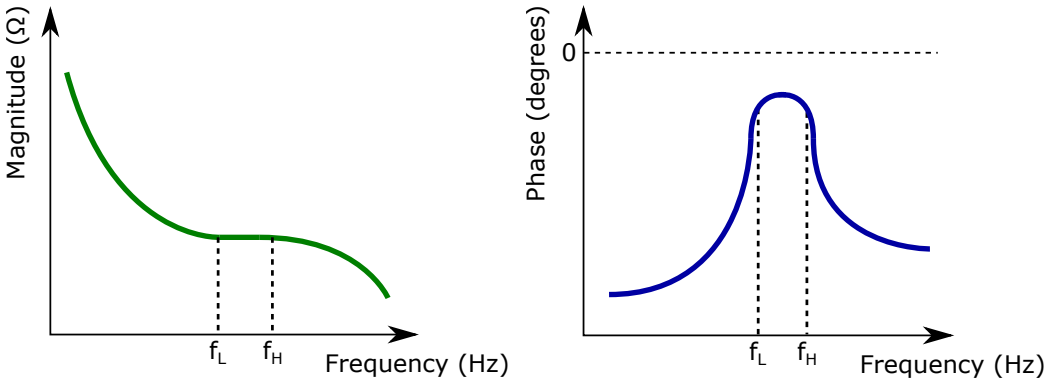

(a) Magnitude frequency response. (b) Phase frequency response.

Figure 2.9: Magnitude and phase frequency responses of the impedance for a coplanar electrode system. There are three distinct regions, separated by the cutoff frequencies f_L and f_H.

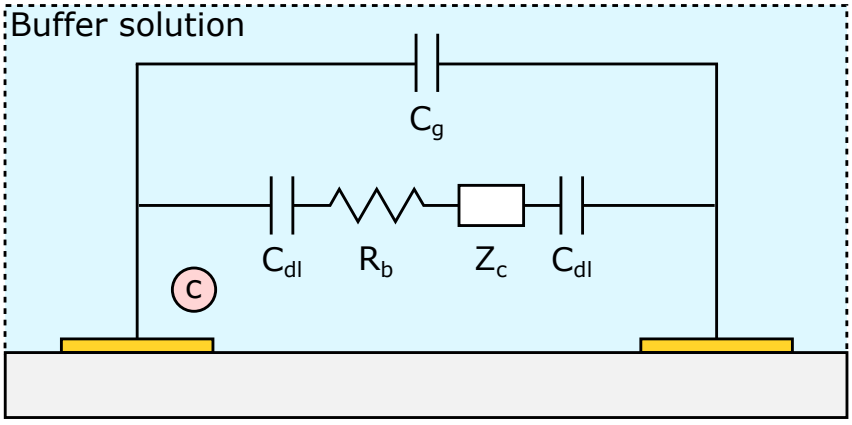

Figure 2.10: Equivalent circuit model for two coplanar electrodes surrounded by a buffer solution modified for a cell (red) passing over the electrodes. The cell adds the impedance element Z_c.

modified to account for the impedance changes introduced by the cell. This can be done by adding a general impedance element Z_c to the circuit, as seen in Figure 2.10. Generally, cells tend to lower the overall impedance magnitude as they increase the system capacitance and are more conductive than the buffer solution. This behaviour is further discussed in Chapter 5.

Chapter 3

Materials and Methods

3.1 Microfluidic platform

3.1.1 Chip fabrication

The following section describes the final fabrication protocol used for the majority of fabricated microfluidic chips. While in the beginning of the project aluminum electrodes were fabricated, this was later changed to gold electrodes as a consequence of their superior characteristics regarding DEP. Both processes are completely interchangeable and described below. A schematic representation is shown in Figure 3.1.

500 μm thick fused quartz substrates with 4-inch diameter were used to fabricate the microfluidic chips using standard photolithography techniques. The substrates were first cleaned in hot piranha solution (3:1 mixture of H_2SO_4 and H_2O_2) for 15 min. For the fabrication of aluminum electrodes, 100 nm of aluminum was sputtered on top of the substrates. The aluminum layer was patterned by spinning the positive photoresist AZ 1512 at 500 rpm for 10 s with a subsequent increase to 5000 rpm for 40s before being baked at 100 °C for 60 s. Substrates were exposed at 100 mJ/cm^2 using an ABM mask aligner (ABM-USA, Inc.) and developed in AZ 400K 1:4 developer. Afterwards, the aluminum layer was etched using metal etchant type A (Transene Company Inc.). Gold electrodes were fabricated using lift-off techniques.[1] LOR 5B

[1] I would like to thank Lian Shoute and Bingxuan Li for their help with fabrication of the gold electrodes. While I originally did all manufacturing steps myself, they manufactured the gold electrodes at the end of the project as well as helped with chip cleaning and dicing.

photoresist (MicroChem Corp.) was spread on the substrates at 500 rpm for 10 s and at 3000 rpm for 40 s and finally baked at 150 °C for 5 min. Subsequently, a second photoresist layer consisting of AZ 1512 was spread on top of the LOR 5B layer, following the same recipe as used for the aluminum electrodes. Afterwards, substrates were exposed to UV light at 100 mJ/cm^2 using an ABM mask aligner. The substrates were then patterned by developing AZ 1512 and LOR 5B layers in AZ developer 1:1 (EMD Performance Materials Corp.) and MF-319 (Kayaku Advanced Materials Inc.), respectively. Lift-off was done in Remover PG (Kayaku Advanced Materials Inc.) after a 10 nm chromium adhesion layer followed by 90 nm gold were sputtered on top of the substrates.

After the fabrication of the electrode structures, the substrates were cleaned with deionized (DI) water to facilitate fabrication of the nanowells. The nanowell structures were created on top of the electrodes with the negative photoresist SU-8 2015 (Kayaku Advanced Materials Inc.). The SU-8 layer thickness and hence the depth of the nanowells used for most of the microfluidic chips was 20 μm. Other thicknesses follow the same process with adjusted process parameters such as spinning speed and exposure energy. A layer thickness of 20 μm was obtained by spreading SU-8 on the substrate at 500 rpm for 5s followed by an increase to 2100 rpm for 30 s. Prebaking of the SU-8 layer was done at 65 °C and 95 °C for 2 min and 4 min, respectively. Afterwards, the nanowell mask was carefully aligned with the substrate using an ABM mask aligner and the substrates were exposed to UV light at 150 mJ/cm^2. Subsequently, the substrates were post-exposure baked at 65 °C and 95 °C for 2 min and 5 min, respectively. Finally, the substrates were developed in SU-8 developer (Kayaku Advanced Materials Inc.) for 4 min. Depending on the design fabricated, the yield per substrate was 6 to 16 chips.

The microfluidic channels required to seal the chip and enable fluidic connection were fabricated with polydimethylsiloxane (PDMS). For this, negative master molds were fabricated on prime silicon wafers with 4-inch diameter. SU-8 2015 was used to form master molds of varying thickness, of which a thickness and hence channel height of 20 μm was used most frequently. The

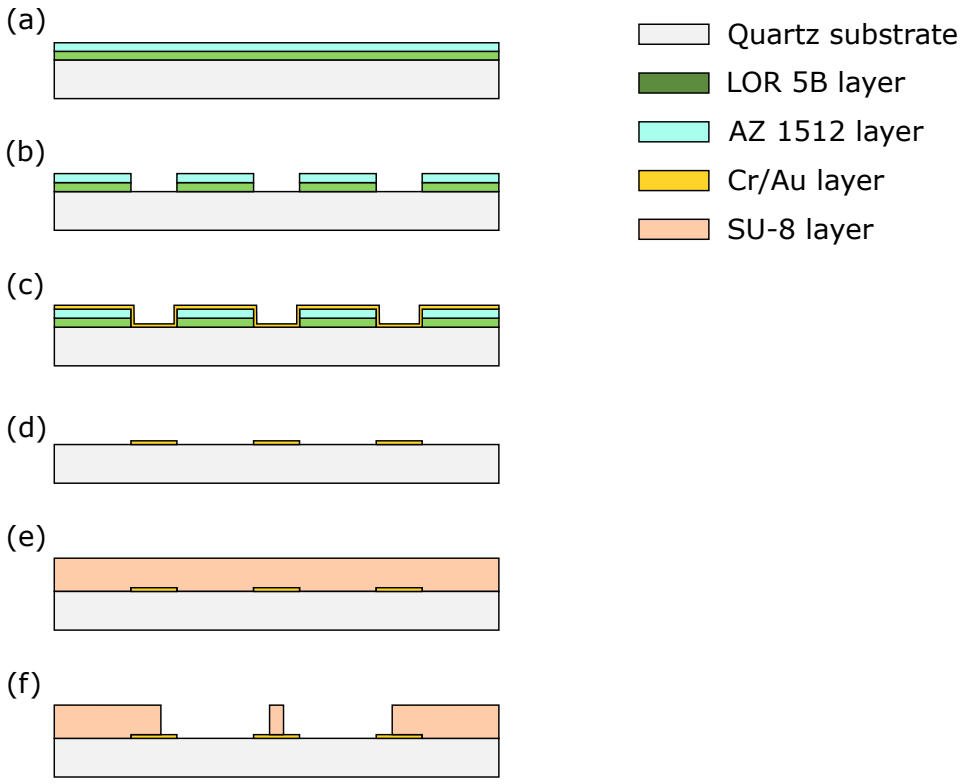

Figure 3.1: Brief overview of the fabrication process flow for microfluidic chips with gold electrodes. LOR 5B and AZ 1512 photoresist are spun on top of the cleaned substrates to form the lift-off layers (a) and subsequently patterned (b). Then, chromium and gold are deposited to form the electrode structures (c) and patterned using lift-off (d). Lastly, the chips are cleaned and SU-8 is spun on the substrates (e) and patterned to form the nanowells (f).

same soft-lithography recipe as described above was used for the master mold fabrication. PDMS with a 10:1 mass ratio between base and curing agent (Sylgard 184 silicone elastomer kit, Dow Inc.) was poured onto the mold and degassed in a desiccator for 30 min. Subsequently, the mixture was cured in an oven at 100 °C for 30 min. Afterwards, the polymerized PDMS was carefully peeled from the mold. A disposable biopsy punch (Robbins Instruments Inc.) was used to create the inlet and outlet holes for microfluidic connection. Lastly, an ultrasound assisted cleaning step with isopropyl alcohol (IPA) and milli-Q water was performed.

3.1.2 Assembly

While thorough cleaning and surface activation of the PDMS microchannel can lead to a strong bond between chip and PDMS, there still is a non-negligible chance that the bond will break partially and the chip will leak. Silanization is an alternative method for device bonding where the microchannel formed by the PDMS structure is irreversibly bonded to the SU-8 layer of the chip. [84]–[86] The bonding process using 99% (3-Aminopropyl)triethoxysilane (APTES) is shown schematically in Figure 3.2. To facilitate bonding, the PDMS side showing the microchannel was first treated and activated with oxygen plasma for 1 min. Immediately after surface activation, the activated side of the PDMS was submerged in APTES for 45 s before being cleaned with milli-Q water. After cleaning, the PDMS was dried with nitrogen gas and carefully aligned with and pressed on top of the microfluidic chip. The complete platform was then placed on a hot plate set to 150 °C for 1 h while a standard calibration weight of 200 grams continued to press the PDMS and chip together to ensure complete sealing. Lastly, 21G stainless steel connectors were inserted into the previously formed inlet and outlet holes of the PDMS and connected to PTFE tubing (Elveflow Microfluidics).

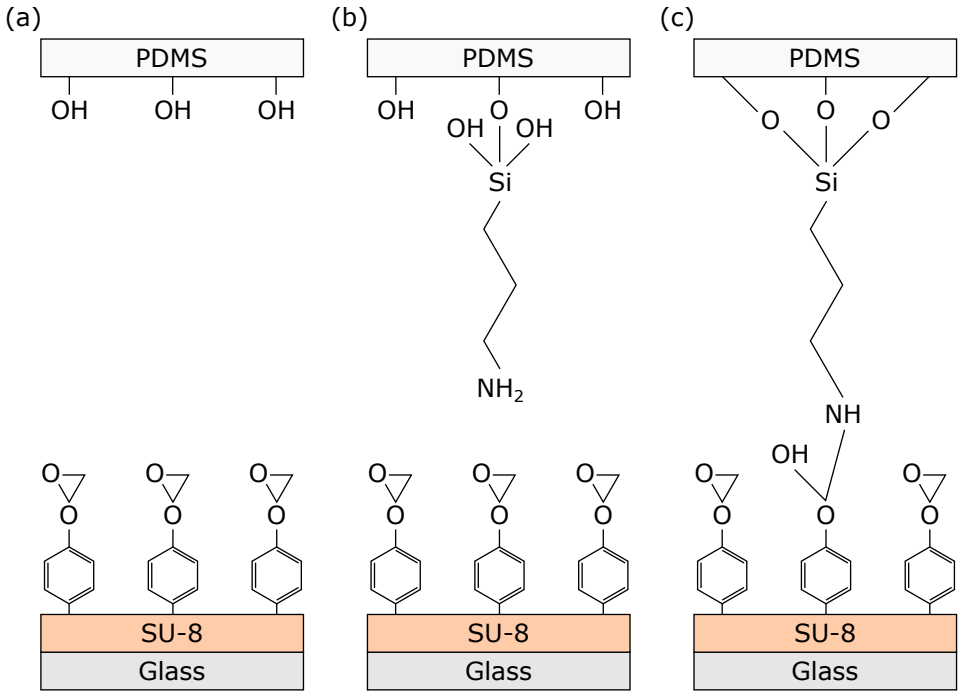

Figure 3.2: Schematic representation of the bonding mechanism between SU-8 layer and PDMS microchannel. The side of the PDMS structure featuring the microchannel is first treated and activated with O_2 plasma, leading to the formation of SiOH groups on the PDMS surface (a). Subsequently, the activated surface is submerged in APTES, which leads to the coupling of APTES molecules to the silanol groups present on the PDMS surface (b). Lastly, the PDMS is brought into contact with the SU-8 layer, where the other end of the APTES molecules bind to the epxoy groups on the SU-8 surface (c).

3.2 Cell preparation

3.2.1 Cell culture

Throughout the project, multiple cell types were used to validate the microfluidic platform. While for proof-of-concept experiments HEK-293T and NIH-3T3 cells were used extensively, later cell sorting trials were conducted using clinically relevant mixed samples consisting of benign (MCF-10A) and malignant (MDA-MB-231) cells.[2] The MDA-MB-231 cells transduced with a doxycycline inducible mEmerald fluorescent vector (MDA-MB-231-Em) to facilitate fluorescence detection. HEK-293T and NIH-3T3 cells were cultured in DMEM medium supplemented with 10% fetal bovine serum (FBS). MDA-MD-231-Em cells were maintained in RPMI-1640 supplemented with 10% FBS, 10 ug/ml puromycin, and 0.5 mg/ml geneticin (Gibco). MCF-10A cells were cultured in DMEM/F12 medium supplemented with 5% horse serum, 100 unit/ml penicillin and 100 mg/ml streptomycin (Gibco), 500 ng/ml hydrocortisone, 20 ng/ml human epidermal growth factor (hEGF), 0.01 mg/ml human insulin, and 100 ng/ml cholera toxin. All cells were cultured in a humidified incubator at 37 °C and a CO2 atmosphere of 5%.[3] All other chemicals used were of analytical grade and obtained from Millipore Sigma.

3.2.2 Cell staining

In preparation for experiments, resuspended HEK-293T and NIH-3T3 cells were induced with 0.7 μL/mL acridine orange for 10 min prior to experiments. MDA-MB-231-Em cells were induced with 2 ug/ml doxycycline for 24 hrs before being detached from the culture plate. MCF-10A cells were detached and stained using the PKH26 red fluorescent cell linker kit for general cell membrane labeling (Millipore Sigma) following the manufacturer's protocol. The

[2]My thanks go to Dr. Judith Hugh and Lacey Haddon for providing the MCF-10A and MDA-MB-231 cells.

[3]I would like to very much thank Lacey Haddon for showing me how to culture and stain cells. Throughout the project, she continued to assist me with cell culture and the majority of more complex cell staining. She also prepared the buffers and media needed. I would also like to thank Zhipeng Yuan for his assistance in maintaining and preparing the cell cultures needed for experiments.

cells were briefly washed once with 1 ml DMEM/F12 and then resuspended in 1 ml diluent C. A 2x PKH26 dye solution was added to the cell suspension and incubated for 5 minutes at room temperature with gentle pipetting. Cells were incubated in 2 ml FBS for 1 minute before being centrifuged at 400 x g for 10 minutes at room temperature. Lastly, stained cells were rinsed 3 times in 5 ml complete media in order to remove excess dye prior to imaging. All cell types were removed from the bottom of the culture plates using 0.25% trypsin-EDTA.

3.2.3 DEP buffer preparation

Since cell media and related buffers generally have a high conductivity, they tend to prohibit a positive DEP response of mammalian cells. To facilitate DEP-based capture and sorting, cells were resuspended in sterile-filtered, low conductivity DEP buffer (10 mM HEPES, 3 mM NaOH, 285 mM sucrose, and 1.5 mM $MgCl_2$) previously used in electroporation studies.[87] After preparation, the conductivity of the buffer was verified with a conductivity meter (Oakton CON 6+) and showed an average read of 500 μS/cm. Cell viability in this buffer has previously been verified by others [87] and was also observed in our experiments. All other chemicals used were of analytical grade and obtained from Sigma-Aldrich.

3.3 Experimental setup

3.3.1 Chip-holder

Several chip-holders were designed throughout the microfluidic platform development. The three key aspects were reliability, cost, and reusability. In the beginning of the project, wires were directly soldered to the pads of the microfluidic chip, although the yield of this was not very high as there was no good adhesion between wires and pads. Next, already available connectors normally used for ribbon cables or flat flex cables (FFC) were explored (Figure 3.3a). The thickness of FFCs is 500 μm and hence satisfies the requirements presented by the substrate height. While these connectors did offer a robust

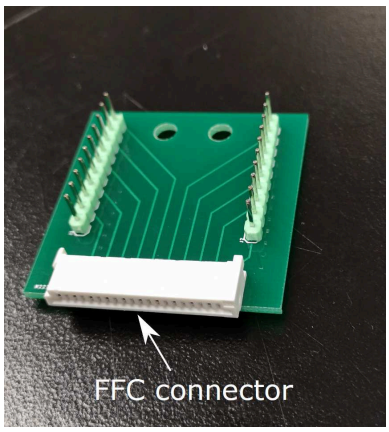

(a) FFC based chip-holder.

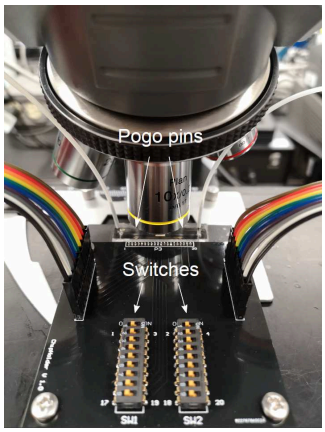

(b) Pogo-pin based chip-holder.

Figure 3.3: Figure 3.3a shows the older version of the chip-holder using FFC connectors, which damages the metal pads on the chip. Figure 3.3b shows the current version of the chip-holder, which uses pogo-pins to connect to the chip. The switches enable internal connection of adjacent traces.

and reliable connection, they also damaged the chip pads with consecutive use. As the physical pins within the FFC connector are very stiff and hard, the thin metal layer that formed the electrode pads was scratched each time a chip was inserted into the connector, eventually leading to complete removal of the metal layer. The next approach, which was used until the end of the project, was a custom-made chip-holder featuring spring-loaded pogo-pins (Mill-Max Mfg. Corp.), as shown in Figure 3.3b. The chip-holder base was designed in Autodesk Fusion 360 and subsequently 3D printed. A custom-made PCB that featured the pogo-pins as well as standard pin headers for connection to external equipment was placed on top of the base.[4] Additionally, the PCB featured a set of switches that enabled the short-circuiting of neighbouring pins, a feature that is useful depending on the chip design. The chip was then inserted between the chip base and pogo-pins and the PCB was subsequently screwed and tightened to the base in order to facilitate connection between chip pads and external equipment. This solution allowed for a reliable and reusable chip connection while at the same time maintaining a low price point.

[4]The original chip-holder was designed by Pedro Duarte for his project. Throughout both our projects, we did modify the original design multiple times to allow newer iterations of our chip designs to fit.

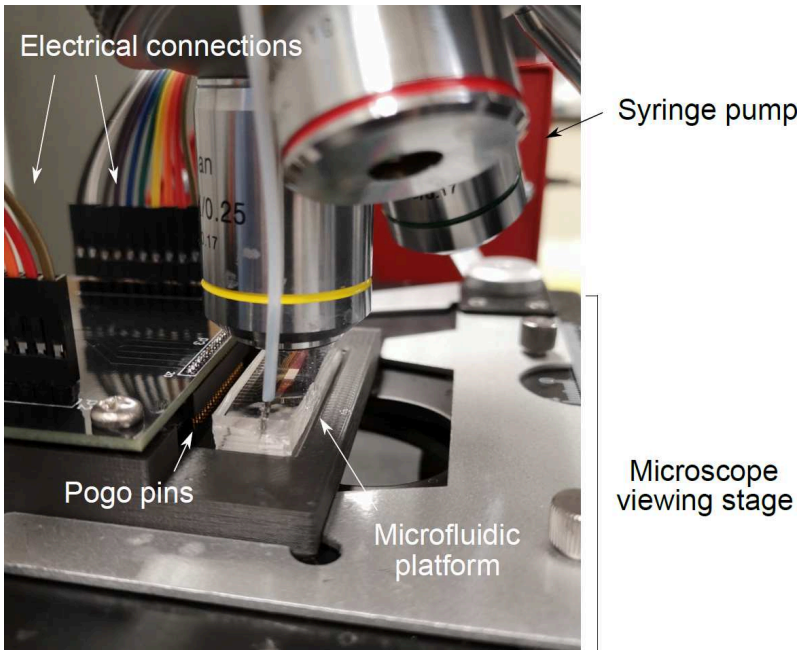

Figure 3.4: Experimental setup showing the chip-holder and microfluidic chip on the microscope viewing stage. The syringe pump (red) can be seen in the background.

3.3.2 External equipment

A syringe pump (New Era Pump Systems Inc. NE-1000) connected to the inlet tubing introduced cell solutions and buffers into the microfluidic channel. DEP capture was facilitated with a function generator (Rigol DG822) connected to a dual-channel 10X amplifier (Tabor Electronics 9250) that applied sinusoidal signals to the electrodes via the chip-holder. Monitoring of the applied signals was done with a digital oscilloscope (Tektronix TDS 2012B). For visual monitoring such as video recording and imaging, the chip-holder was placed on the viewing stage of an upright fluorescence microscope (Amscope FM820TMF143) integrated with a CCD camera (Sony ICX825ALA) to enable visual monitoring such as imaging and video recording. Figure 3.4 shows the fluidic side of the experimental setup. EIS measurements were conducted using a high-precision impedance analyzer (Zurich Instruments MFIA) controlled by LabOne software.

Chapter 4

Development of cell sorting platform

4.1 Proof-of-concept experiments and designs

4.1.1 First iteration of the microfluidic platform

First, a nanowell chip with a small number of wells was designed to validate DEP-assisted cell capture. The chip, as seen in Figure 4.1, consisted of 20 separate coplanar aluminum electrodes that formed 10 arrays seated within a 800 μm wide microchannel. On top of each array, 10 nanowells were fabricated using the negative photoresist SU-8. Each wafer yielded 16 chips, equally divided into chips with diameters of 10 μm, 15 μm, 20 μm and 25 μm. The gap between a pair of electrodes was 4 μm for 10 μm wells, 5 μm for 15 μm wells, and 6 μm for both 20 and 25 μm wells. Lastly, the microfluidic chips were sealed with PDMS covers and connected to external equipment.

Validation experiments were conducted with polystyrene beads as well as *Sclerotinia sclerotiorum* spores.[1]

4.1.2 Preliminary results and discussion

While DEP capture generally worked after signal frequency and amplitude were tuned to the respective particle, there were a number of issues encountered with this first design. First iterations were missing alignment marks that were

[1]I would like to thank Pedro Duarte and Riley Stuermer for their help in assisting me with these validation experiments. Spores were generously provided by Dr. Xiujie S. Li from InnoTech Alberta and maintained by Pedro Duarte.

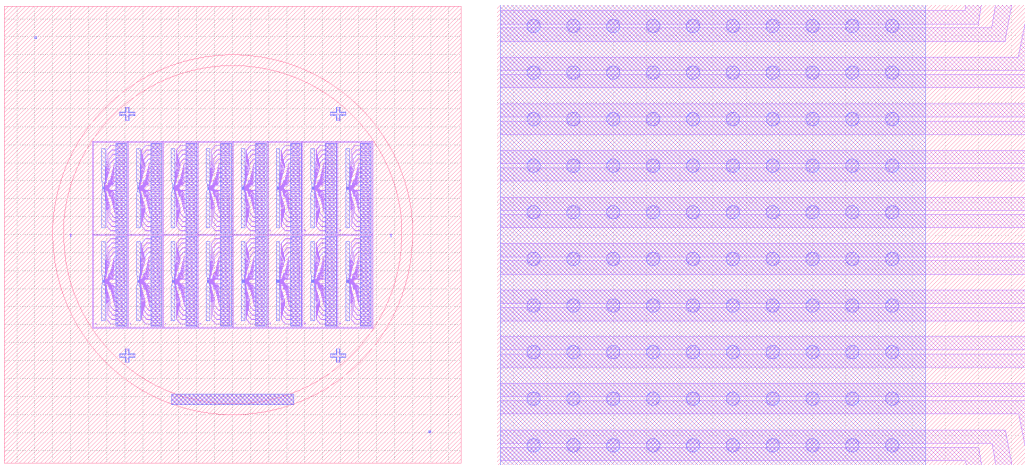

(a) (b)

Figure 4.1: Design of the microfluidic chips used for proof-of-concept experiments. Figure 4.1a shows the overall mask design. Figure 4.1b provides a close-up of the electrode array structure with 20 μm wells.

small enough to allow for the exact alignment of nanowells and electrodes. As a result, some chips featured misaligned layers which only enabled limited or no DEP capture (Figure 4.2a). Additionally, the nanowells were placed rather far apart from each other and only along a few lines normal to the electrodes, with no variation in position between separate arrays. Due to the overall laminar flow particles did not change their initial trajectory in the microchannel and thus ended up partially not crossing any wells at all, which led to a significant decrease in capture performance.

Another phenomenon that was observed with aluminum electrodes was an issue subsequently referred to as electrode "burning". When buffer solutions with higher conductivity, i.e. cell culture buffers, were flowed through the chip, bubbles immediately formed at the electrodes and electrodes started to rapidly dissolve once the DEP signal was turned on (Figure 4.2b)[2]. Turning off the DEP signal stopped the process and bubbles could subsequently be flowed out of the chip. Measuring the temperature of the effected area with a handheld IR-temperature meter revealed an immediate increase of 6 °C over ambient temperature. As the laser of the IR meter was quite big compared to the electrodes and hence gave the average temperature of a larger area, the

[2]I would like to thank Riley Stuermer for providing this image.

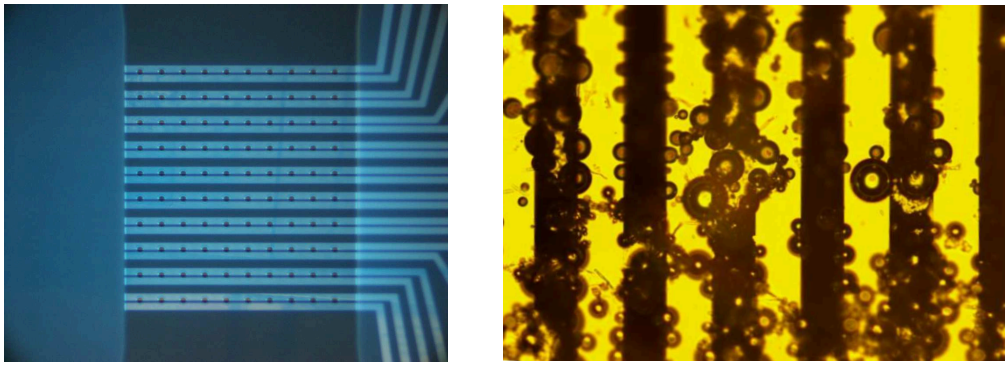

(a) (b)

Figure 4.2: Problems encountered with the proof-of-concept design. Figure 4.2a shows the occasionally occurring alignment problems between the metal and SU-8 layer caused by the absence of alignment markers accurate enough to resolve the necessary dimensions. Figure 4.2b shows bubble build-up at electrodes seen when flowing high-conductivity buffers.

temperature at the electrodes themselves most likely had a much higher value. This indicated that the increase in medium conductivity led to a subsequent increase in current. Looking at the well known equation for electric power

$$P = V * I = \frac{V^2}{R} \tag{4.1}$$

where V is the applied voltage, I the electric current, and R the resistance of the introduced buffer solution, we can see that the power and hence the energy needed to be dissipated by the electrodes and fluid rose with a decrease in buffer resistance. Once a certain threshold was reached, the thermal capabilities of the electrodes and buffer could no longer dissipate the generated heat and the electrodes started to burn.

The chip burning phenomenon was not further examined in this thesis, as a change of electrode metal to gold as well as adjustment of the used buffer prevented this issue from occurring again.

4.2 Development of multisectorial platform

Based on the results and insights gained from the proof-of-concept designs, the current cell sorting platform was designed. The issues encountered with the proof-of-concept chips were solved by incorporating design changes and careful buffer consideration. Additionally, the chip was expanded to feature a greater number of nanowells through tighter packed nanowells and the use of interdigitated electrodes (IDEs). The next sections provide details about the platform design, capture performance, and cell sorting performance.

4.2.1 Design and operating principle

The microfluidic platform (Figure 4.3a) was designed and fabricated with a total of 10 individually addressable sectors. Each sector contains an interdigitated electrode structure formed by 20 coplanar gold interdigitated nanoelectrodes with a thickness of 100 nm (90 nm gold on 10 nm chromium). The nanoelectrodes are 14 μm wide and are separated from each other by a 6 μm gap, which is also the gap spacing between adjacent sectors. On top of each IDE sector, 1000 nanowells made of SU-8 photoresist were placed in a 50 by 20 nanowell matrix, resulting in a total nanowell count of 10 000 per chip (Figure 4.3b). The nanowells were placed in a pattern akin to hexagonal packing to ensure that cells flowing horizontally across the chip would always pass over a minimum number of nanowells. As shown in Figure 4.4a, this particular placement enabled cell capture independent from the initial y-position of the target cell. A microfluidic channel distributed fluid and cell flow evenly across the entire chip and connected inlet and outlet ports.

Since cell sizes vary greatly depending on their phenotype, it is important to identify the target cell size during the design stage and adjust the nanowell size accordingly. Ideally, after considering size variations within their own population, only a single cell should fit into each nanowell. The target cell lines for this study, MDA-MB-231 and MCF-10A, have been reported to generally have a diameter between 11 μm and 19 μm.[88], [89] The cultured cells showed an average diameter of 14 μm for MDA-MB-231 cells and 17 μm for MCF-10A

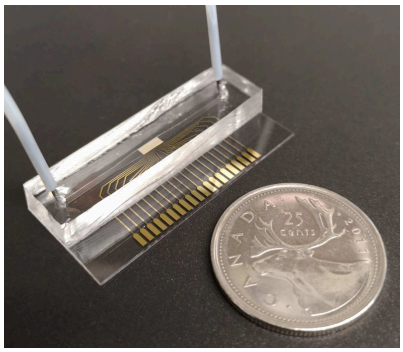

(a)

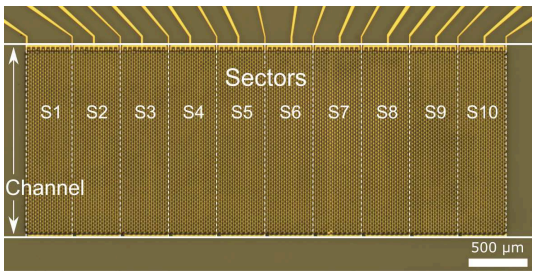

(b)

Figure 4.3: Design and assembly of the microfluidic platform. Figure 4.3a: Assembled microfluidic platform. Figure 4.3b: Microscopic image of the nanowells and interdigitated electrodes (IDEs). Each of the 10 individually addressable sectors contains 1000 nanowells, resulting in 10 000 nanowells per chip.

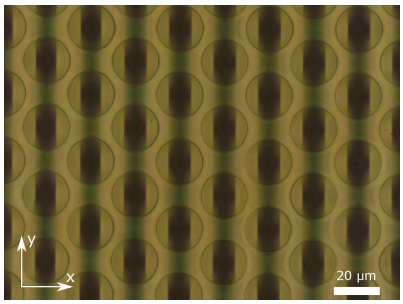

(a)

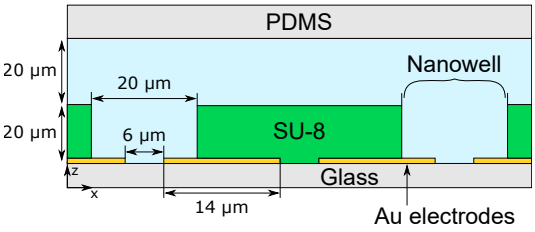

(b)

Figure 4.4: Design of the nanowell structure of the microfluidic platform. Figure 4.4a shows a microscopic close-up image of the nanowells and IDE structures. Figure 4.4b shows a cross-sectional schematic representation of the assembled platform (not to scale).

cells. Based on these results, chips with a nanowell diameter and depth of 20 μm were fabricated (Figure 4.4b).

To generate the non-uniform electric field necessary for DEP capture, a sinusoidal voltage was applied to the IDEs through a custom-made chip holder (Figure 3.3b). The chip holder allowed for the application of individual signals to each sector but could also be externally configured to apply the same signal to an arbitrary number of adjacent sectors via the routing switches (Figure 4.5a). After cell loading and capture, non-faradaic electrochemical impedance spectroscopy (nF-EIS) was used in combination with fluorescence imaging to monitor the cell occupancy of the sector under test. Similar to DEP capture,

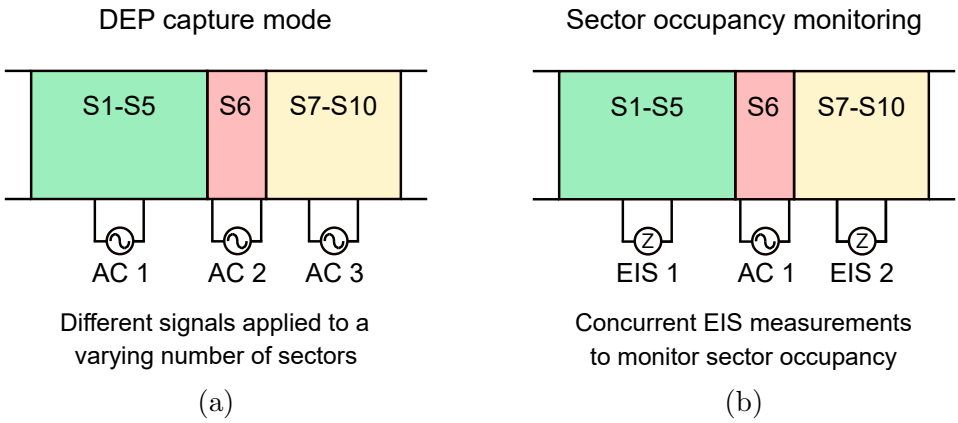

Figure 4.5: Operating modes of microfluidic platform. Each sector can be operated individually or combined with adjacent sectors to capture a specific cell type (Figure 4.5a). Each sector or number of adjacent sectors can be also operated in electrochemical impedance spectroscopy (EIS) measurement mode to monitor the sector occupancy (Figure 4.5b). This can be done while other sectors are still operated in DEP capture mode.

nF-EIS measurements could be taken of either a single sector or an arbitrary number of adjacent sectors, depending on the routing switch setting (Figure 4.5b). Note that nF-EIS measurements of any selected sectors can be taken while the remaining sectors are still operating in DEP capture mode.

4.2.2 Dielectrophoresis-assisted cell capture

First, the cell capture performance of the microfluidic platform was evaluated. For this purpose, two sets of experiments examining the dependencies of flow rate and applied voltage on cell capture were designed on chips with 20 μm nanowell diameter. All experiments were repeated three times on three different chips. Before loading cells, the chips were primed by slowly injecting 250 μL of ethanol at a flow rate of 10 μL/min to remove air bubbles from within the nanowells. Subsequently, 250 μL of DEP buffer were flowed through the channel to remove the excess ethanol. Then, a homogeneous 5.5 μL sample of viable MDA-MB-231 cells resuspended in DEP buffer was introduced into the chip with varying flow rate and DEP capture voltage conditions. Cells were counted and prepared to be at a concentration of 200 cell/μL, resulting in a total number of 1100 cells per injected cell sample. This number is 10% higher

than the number of nanowells per sector and was chosen to account for potential cell loss during sample transfer and sample introduction into the chip. To enhance visibility, cells were stained with the fluorescent dye acridine orange 10 min prior to loading. After the entire sample volume had passed through the chip, a washing step removing any cells not captured in nanowells was performed by injecting DEP buffer for 3 min at a flow rate of 75 μL/min. The DEP signal stayed turned on during the washing step to ensure that captured cells did not leave their respective nanowell.

Influence of flow rate on cell capture performance

In the first set of experiments, cell samples were introduced at varying flow rates of 0.5 μL/min, 0.8 μL/min, and 1 μL/min while the amplitude of applied sinusoidal capture signal was kept at a peak-to-peak voltage 15 V_{pp} and 1 MHz. Initial test runs showed that nanowells were predominantly found in one of the following states of occupancy: a 0-cell state (in which no cell was captured and the nanowell is empty), a 1-cell state (in which a single cell was captured by a particular nanowell), and the less likely 2-cell and 3-cell states (following the same nomenclature).

As shown in Figure 4.6a, a high cell occupancy was observed at a flow rate of 0.8 μL/min, with cells in the 1-cell state occupying 636 nanowells and cells in the 2-cell state occupying 130 nanowells. 228 nanowells were empty at a flow rate 0.8 μL/min, whereas for flow rates of 0.5 μL/min and 1 μL/min, the number of empty nanowells increased to 305 and 346, respectively. For a flow rate of 0.5 μL/min, this behavior can be explained by the higher rate of occurrence of multiple cells being captured in the same nanowell (Figure 4.6b). 32.81% of captured cells were in a 2-cell state and 8.61% in a 3-cell state. The 3-cell state only occurred at a significant rate for a flow rate of 0.5 μL/min, while it could rarely be seen for 0.8 μL/min and 1 μL/min ($p=0.0005$, one-way ANOVA).

At a lower flow rate, cells are subjected to F_{DEP} for a longer time when passing over a nanowell and hence are more likely to get captured in that nanowell. Similarly, higher flow rates imply an increase in average cell velocity

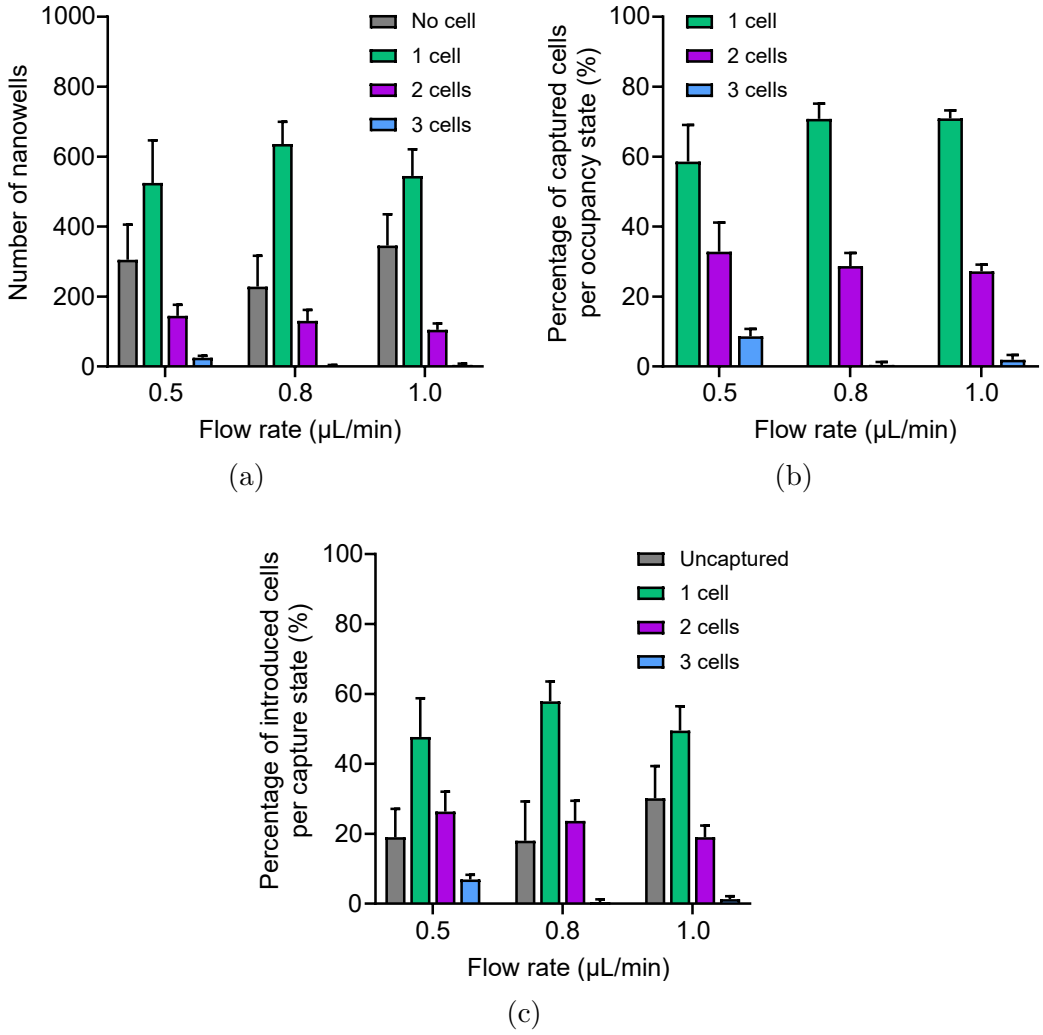

Figure 4.6: Sector occupancies obtained at different flow rates and a fixed DEP signal amplitude of 15 V_{pp} after 1100 cells were introduced into the platform. Each bar shows the mean and standard deviation of three independent experiments repeated on different sectors. The total number of nanowells per sector was 1000. Occupancy states for any particular nanowell generally range from no captured cells to three captured cells. (4.6a) Sector occupancy states. (4.6b) Distribution of occupancy states. (4.6c) Capture state distribution for all introduced cells.

which causes a decrease in capture probability. This behaviour could be seen by looking at the increased number of empty nanowells observed at a flow rate of 1 μL/min when compared to 0.8 μL/min (Figure 4.6a) while the occupancy state distribution among the captured cells was similar between the two experiments (Figure 4.6b).

The overall capture efficiency with respect to the total number of introduced cells is shown in Figure 4.6c. At a flow rate of 0.8 μL/min, the percentage of uncaptured cells was 18.00%, which was similar to 19.03% seen at a flow rate of 0.5 μL/min and lower than the 30.18% observed at a flow rate of 1 μL/min. Lastly, the percentage of captured cells in the 1-cell state was highest at a flow rate of 0.8 μL/min with a value of 57.85%, compared to 47.70% and 49.51% at flow rates of 0.5 μL/min and 1 μL/min, respectively.

Influence of signal amplitude on cell capture performance

The second set of experiments examined the dependency between cell capture and applied DEP signal amplitude. Based on the results obtained from the first set of experiments, cell samples were loaded into the chip at a constant flow rate of 0.8 μL/min while the DEP signal amplitude was set to 10 V_{pp}, 15 V_{pp}, and 20 V_{pp}. As seen in Figure 4.7a, experiments with signal amplitudes of 10 V_{pp} and 20 V_{pp} both showed a significant number of empty nanowells with 420 and 431 empty nanowells, respectively, opposed to the 228 empty nanowells seen at 15 V_{pp} (p=0.027). While measurements at 15 V_{pp} exhibited the highest number of nanowells in a 1-cell state at 636 wells, analysis of the captured cells revealed that at 10 V_{pp}, 90.15% of captured cells were found in a 1-cell state (Figure 4.7b). This percentage significantly decreased to 70.82% with an increase in capture signal amplitude to 15 V_{pp}, and to 50.57% at 20 V_{pp} (p=0.007). Similarly, the percentage of captured cells in a 2-cell state increased considerably with the signal amplitude, from 9.84% at 10 V_{pp}, over 28.69% at 15 V_{pp}, to 39.24% at 20 V_{pp}. Additionally, experiments with an amplitude of 20 V_{pp} showed a notable occurrence of the 3-cell state. To examine this behaviour further, finite element simulations of a single nanowell were performed in COMSOL Multiphysics 5.5.

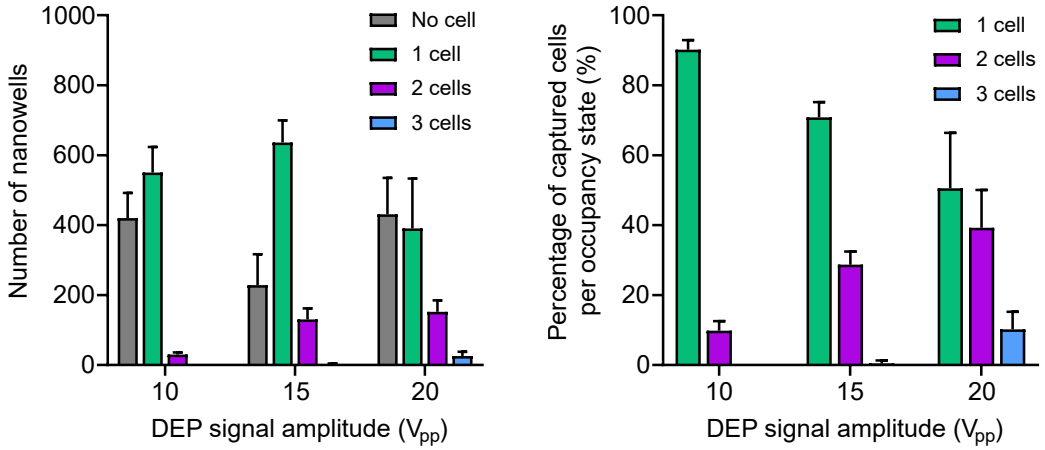

(a)

(b)

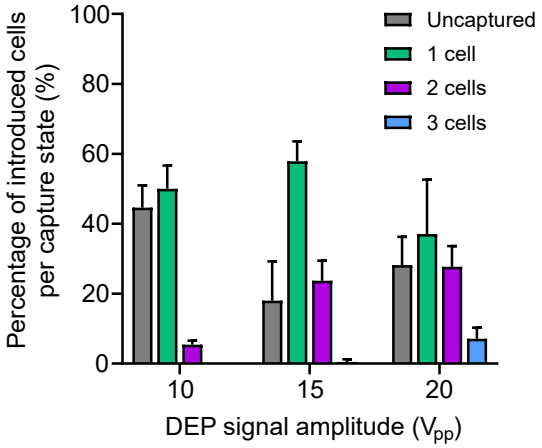

(c)

Figure 4.7: Sector occupancies obtained at different DEP signal amplitudes and a fixed flow rate of 0.8 μL/min after 1100 cells were introduced into the platform. Each bar shows the mean and standard deviation of three independent experiments repeated on different sectors. The total number of nanowells per sector was 1000. Occupancy states for any particular nanowell generally range from no captured cells to three captured cells. (4.7a) Sector occupancy states. (4.7b) Distribution of occupancy states. (4.7c) Capture state distribution for all introduced cells.

COMSOL simulations of channel height

Figure 4.8a shows the simulation domain and electric field generated by a pair of coplanar nanoelectrodes with the electric field magnitude $|E|$ being expressed by a colour map. As described in Equation 2.1, the DEP force acting on a particle is directly proportional to the gradient of the squared electric field $\nabla|E|^2$. We define the effective field gradient as

$$\nabla|E|^2_{eff} := \int \nabla|E|^2 dA \tag{4.2}$$

where A represents the cross-sectional area above the nanowells over which the electric field gradient is integrated and is shown as the white-dashed rectangle in Figure 4.8a. The area was fixed at a height of 10 μm and nanowell diameter of 20 $_{\text{pp}}$m. The relationship between effective field gradient and distance normal to the nanowell surface for different applied voltages is shown in Figure 4.8b. For higher distances from the nanowell surface, the electric field gradient and thus DEP force drops asymptotically to zero. This suggests that cells should optimally be constrained by the chip geometry to flow as close to the nanowells as possible and stresses the importance of taking cell diameter into account when designing channels. As the applied voltage increases, the gradient and thus the DEP force acting on particles increases as well. Consequently, higher field amplitudes result in a higher overall capture efficiency. This implies that at 20 V_{pp} the overall percentage of captured cells should be highest out of all experiments.

However, Figure 4.7c shows that the percentage of uncaptured cells at 20 V_{pp} was 28.18%, which, while being lower than 44.61% as observed at 10 V_{pp}, is still higher than the measured 18.00% of uncaptured cells at 15 V_{pp} (p=0.27). This behaviour can be explained by the observation that a higher signal amplitude causes more cells to be attracted to a single nanowell. Since the nanowells were designed to ideally only hold a single cell each, subsequently attracted cells did not fit completely into already occupied nanowells and ultimately formed clusters on top of the SU-8 nanowell layer. At low flow rates, the adhesion of cells to each other supported by the DEP force allowed cells

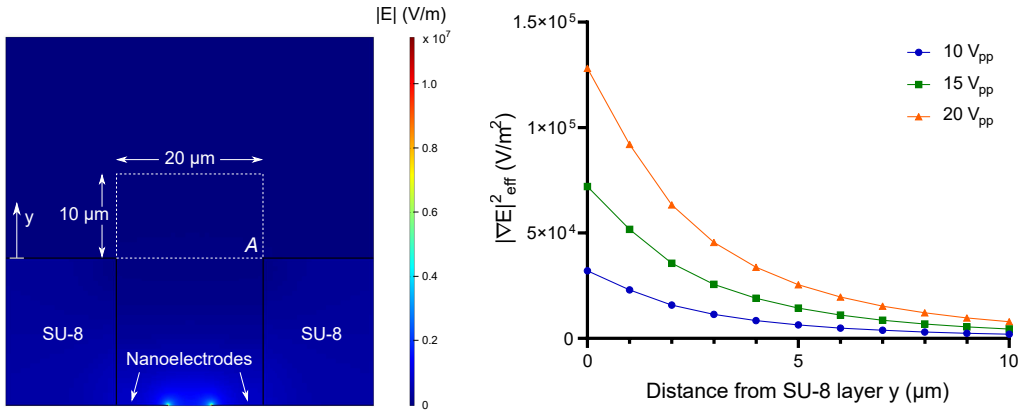

(a) (b)

Figure 4.8: COMSOL Multiphysics simulations of channel height. Figure 4.8a shows the simulation domain and colour map of the electric field generated by the nanoelectrodes. The white dashed rectangle A shows the integration area required to calculate the effective field gradient expressed by Equation 4.2. Figure 4.8b shows the simulation results of the effective field gradient plotted against the distance from the SU-8 layer for different values of the applied V_{pp}. The effective gradient decreases exponentially as the integration area moves further away from the electrodes. Therefore, the strength of the DEP force acting on cells that flow higher in the microfluidic channel decreases as well.

to stick together. However, during the washing step, the flow rate increased significantly, causing the clusters to be washed away. Therefore, even though the initial capture performance of 20 V_{pp} was very good, subsequent steps released the cells, which is unwanted for reliable cell sorting.

Consequently, a compromise between signal amplitude and flow rate had to be made. Based on the aforementioned results, a flow rate of 0.8 μL/min and DEP signal amplitude of 15 V_{pp} were chosen and used in all subsequent experiments, unless otherwise noted. This set of parameters showed the most promising results for overall capture rate as well as single cell capture rate per sector with 82.00% and 57.85%, respectively. Images of sectors and their final occupancies at different flow rates and DEP capture voltages are shown in Figure S3.

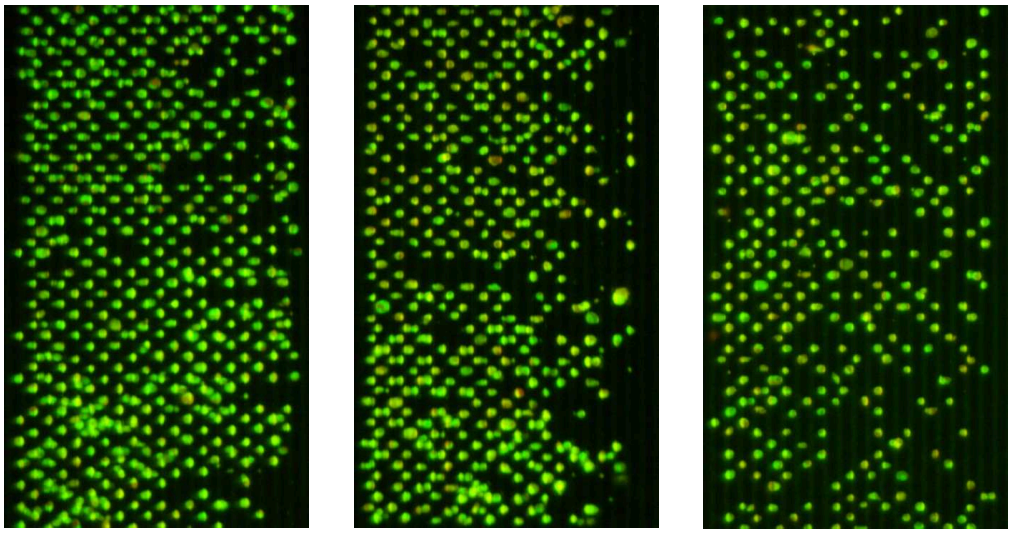

(a) (b) (c)

Figure 4.9: Fluorescent images of captured MDA-MB-231 cells stained with acridine orange at different flow rate and DEP signal amplitude settings. The signal frequency was fixed at 1 MHz. (4.9a) Flow rate of 0.8 μL/min and a DEP signal amplitude of 15 V_{pp}. (4.9b) Flow rate of 1.0 μL/min and a DEP signal amplitude of 15 V_{pp}. (4.9c) Flow rate of 0.8 μL/min and a DEP signal amplitude of 10 V_{pp}.

4.2.3 Dielectrophoresis-assisted cell sorting

To evaluate the cell sorting performance of the platform with a clinically relevant mixed sample, several experiments were designed. As seen in equation 1, the direction of DEP force follows from the frequency dependence of the CM factor and hence varies for different cell types at a given frequency. Therefore, it is possible to facilitate DEP based cell sorting by tuning the frequency in such a way that only one cell type is attracted towards the nanowells. In the first experiment, the DEP signal settings were chosen to enable capture of all introduced cells in the sectors where the signal was applied (Figure 4.10a). Contrary to that, the second experiment was aimed at sorting the two cell types by adjusting the DEP signal frequency so that only one cell type would be captured in the nanowells (Figure 4.10b). Lastly, a third control experiment that applied different DEP signals to two separate groups of sectors was conducted. Whereas the signal applied to the first group of sectors only enabled DEP capture of a single cell type, a signal facilitating capture of both

cell types was applied to the subsequent group of sectors (Figure 4.10c).

A mixed sample of MDA-MB-231 and MCF-10A cells, in the following paragraph referred to as 231-cells and 10A-cells, was prepared at a final concentration of 100 cells/μL. To allow for optical detection, 231-cells transduced with the mEmerald green fluorescent protein and 10A-cells stained with the red fluorescent cell linker PKH26 were combined at a 1:1 ratio.[3] Cells were injected into the chip at a flow rate of 0.8 μL/min while a DEP signal with an amplitude of 15 V_{pp} was applied. To determine the frequency range required for successful DEP sorting, the real part of the CM factor was calculated and plotted for both cell types (Figure 4.11). Cells were modelled with a single-shell model and with dielectric parameters reported in [69], [70], [90]. The dielectric parameters are shown in Table 4.1 with detailed parameters listed in Appendix A. As shown in Chapter 2, the cytoplasm permittivity generally is very similar between different cell types with the membrane conductivity being low.[72], [73], [91] Additionally, changes in these two parameters do not affect the CM factor curve much since the shape of the curve mainly depends on cytoplasm conductivity and membrane permittivity. Hence, both cell types show the same cytoplasm permittivity and membrane conductivity.

Parameter	MDA-MB-231	MCF-10A
$\varepsilon_{r,cytoplasm}$	60	60
$\sigma_{cytoplasm}$ (S/m)	1.17	1.40
$\varepsilon_{r,membrane}$	6.13	13.36
$\sigma_{membrane}$ (S/m)	$1 * 10^{-6}$	$1 * 10^{-6}$

Table 4.1: Dielectric parameters of MDA-MB-231 and MCF-10A cells. [69], [70], [90]

There is a clear difference between the frequency responses of the CM factor with the value for 10A-cells turning positive well before the 231-cells. Moreover, the curve obtained for 10A-cells is strictly higher than the curve for 231-cells for positive values, indicating that it is very unlikely to capture 231-cells without also capturing 10A-cells. Based on the plot, a frequency

[3] I would like to thank Lacey Haddon for providing the transduced 231-cells as well as making the cell linker work with 10A-cells.

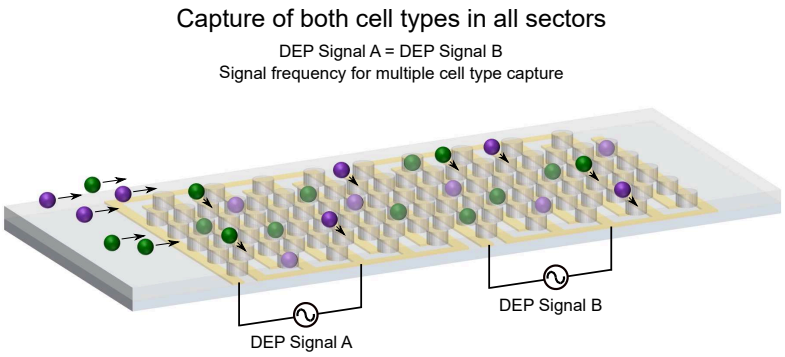

(a)

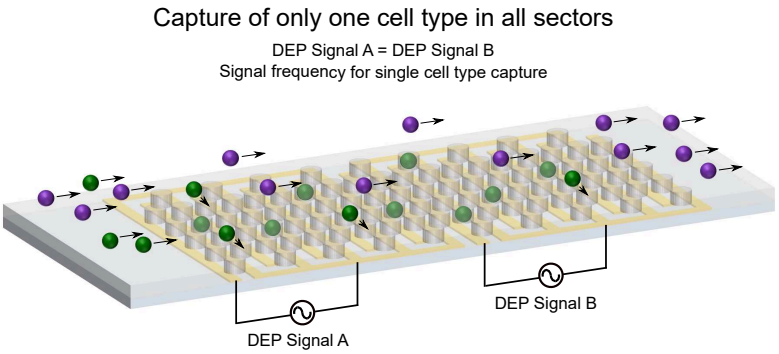

(b)

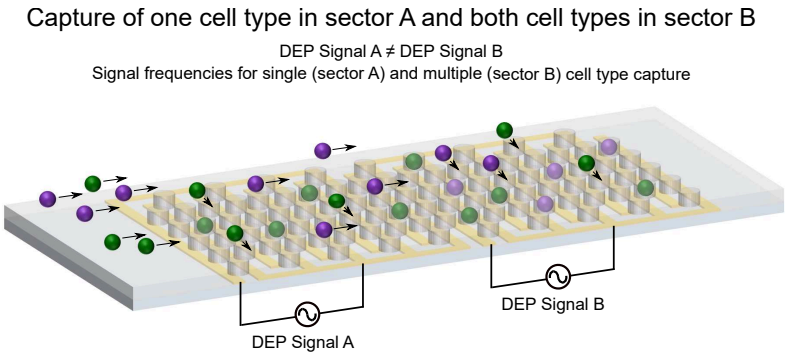

(c)

Figure 4.10: Schematic representation of experiments evaluating the cell sorting performance of the platform. (4.10a) Both cell types are captured in both sectors as the same signal with a frequency facilitating multiple cell type capture is applied to both sectors. (4.10b) Only one cell type is captured in both sectors, therefore sorting the sample. The same signal with a frequency tuned to capture only one cell type is applied to both sectors, causing the uncaptured cell type to exit the chip. (4.10c) Control experiment that first captures only one cell type in the first sector and subsequently both cell types in the second sector. Different signals are applied to both sectors to enable this behaviour.

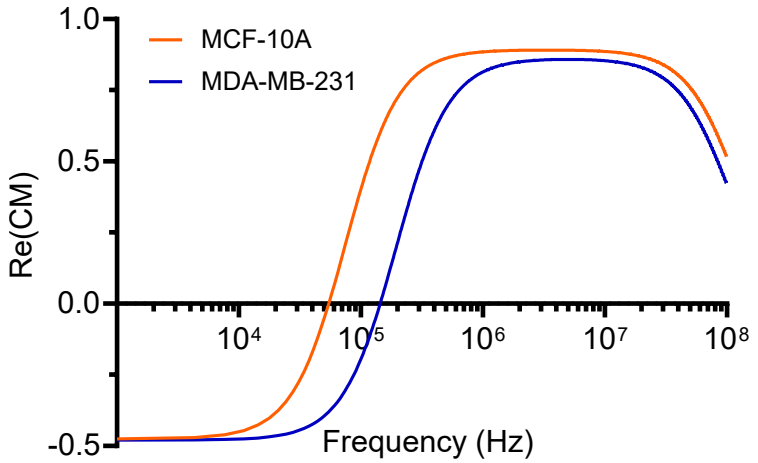

Figure 4.11: Real part of the CM factor for both MDA-MB-231 and MCF-10A cells plotted against the frequency.

of 250 kHz was chosen for exclusive capture of 10A-cells (Figure 4.12a). At this frequency, the CM value of 10A-cells begins to decrease in slope as it approaches the maximum value which it reaches at around 500 kHz. The CM value for 231-cells at this frequency, while also positive, is too small to enable cell capture. Furthermore, a frequency of 1 MHz was chosen for control measurements as at this value both curves are close to their respective maxima. Hence, both cell types are captured and trapped in nanowells at this frequency (Figure 4.12b).

Accuracy of selective single-cell sorting

The previously described experiments were conducted three times on different chips with the chosen frequencies of 250 kHz and 1 MHz. Measurements were taken at different sector occupancies and injection times to provide for a time and occupancy-independent performance analysis. As seen in Figure 4.13a, when a DEP signal with a frequency f_{DEP} of 1 MHz was applied to the sectors, the percentages of captured 10A-cells and 231-cells were 76.72% and 23.28% on average, respectively. This is attributed to two inherent differences between the cell types, the CM value as well as the average cell diameter. 10A-cells have a higher CM value and were measured to have a larger diameter than 231-cells and therefore experience a stronger DEP force (Equation 1). At an f_{DEP} of 250 kHz, it was observed that 95.2% of captured cells were 10A-cells,

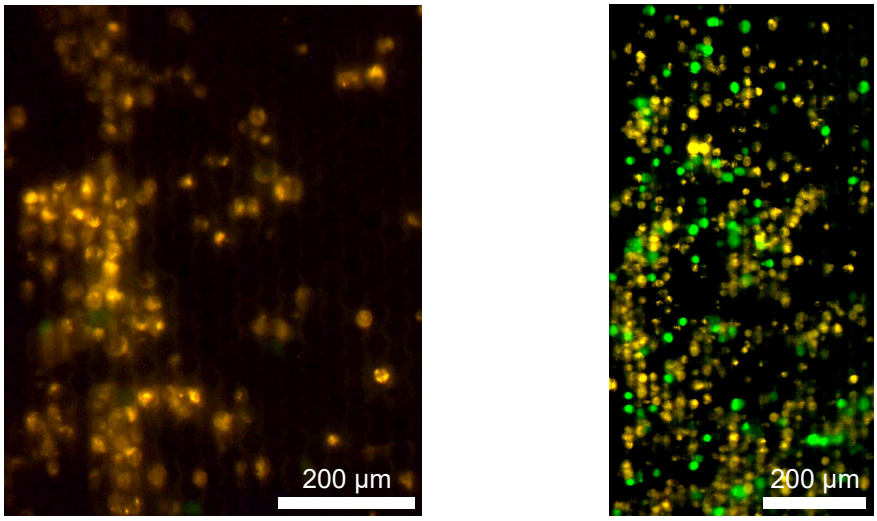

(a) (b)

Figure 4.12: (4.12a) Fluorescent image taken with DEP settings for exclusive capture of 10A-cells. 10A-cells appear yellow. (4.12b) Fluorescent image taken with DEP settings for capture of both 231-cells and 10A-cells. 10A-cells appear yellow, and 231-cells appear green.

as the CM value for 231-cells is significantly lower at this frequency than the CM value for 10A-cells (Figure 4.13b).

In the third experiment, two varying f_{DEP} values were applied to different sectors of the chip. In a control run, an f_{DEP} of 1 MHz was applied to one sector followed by an f_{DEP} of 3 MHz applied to the other sector. The capture distributions on both sectors were very similar with 10A-cell and 231-cell capture percentages of 77.92% and 22.08% on the first, and 77.99% and 22.01% on the second sector (Figure 4.14a). This behaviour is expected because there is minimal change in the CM value for either cell type for frequencies in this range. Lastly, an f_{DEP} of 250 kHz was applied to one sector on the chip to selectively capture only 10A-cells while an f_{DEP} of 1 MHz was applied to later sectors to facilitate capture of all remaining cells (Figure 4.14b). Similar to previous results, 95.84% of captured cells in the first sector were 10A-cells while the percentages of 10A-cells and 231-cells in the later sectors were 71.67% and 28.33%. This slight shift in the distribution is due to 10A-cells being trapped in nanowells in the first sector, leading to a decrease of 10A-cells present in later sectors. Lastly, the nanowell occupancies observed for both cell types

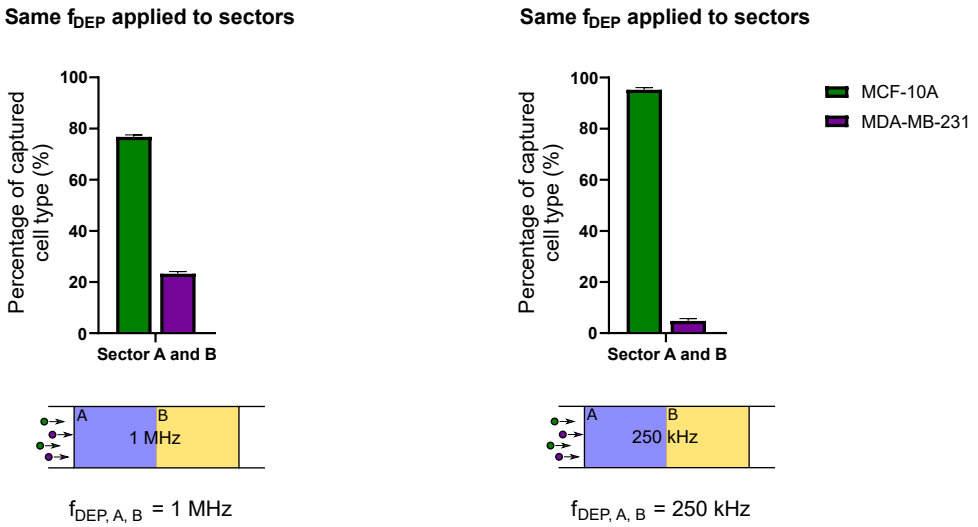

Figure 4.13: Cell sorting performance for different sector and frequency configurations. In Figure 4.13a the frequency applied to both sectors is 1 MHz, whereas in Figure 4.13b it is 250 kHz. Hence, in the latter only MCF-10A cells are captured.

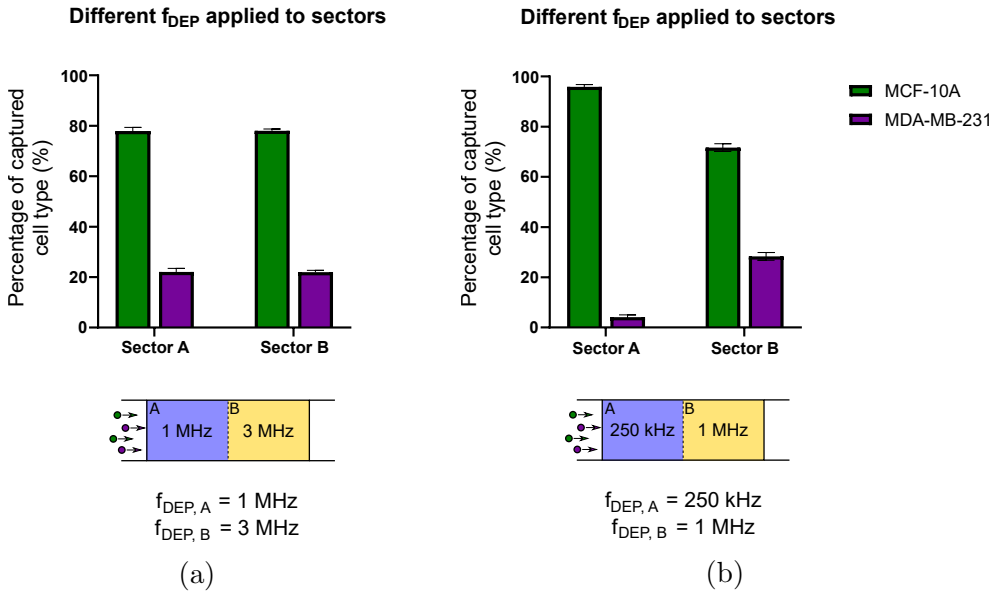

Figure 4.14: Cell sorting performance for different sector and frequency configurations. In Figure 4.13a the frequency applied to sector A is 1 MHz and the one applied to sector B is 3 MHz. In Figure 4.13b the frequency applied to sector A is 250 kHz and the one applied to sector B is 1 MHz, facilitating exclusive capture of MCF-10A cells in sector A.

at f_{DEP} values of 1 MHz and 3 MHz were very similar to the ones discussed earlier since the same flow rate and DEP signal magnitudes were used. The occupancy observed for 10A-cells at 250 kHz decreased as the CM factor and therefore the strength of the DEP force decreased as well. According to these results, it is evident that the microfluidic platform can be employed to selectively sort and trap single cells.

4.3 Conclusion

In this chapter, a microfluidic platform based on a multisectorial electroactive nanowell structure was presented. Selective cell sorting of complex samples is essential in a multitude of biomedical applications. Hence, it is important to develop a device that can be quickly and easily modified to sort any types of cells. The microfluidic platform aims to fulfill these criteria by using dielectrophoresis to sort and capture cells in 10 individually addressable sectors. The unique sector structure allows for easy multi-stage designs and modifications to sort more complex samples. The feasibility of the platform to selectively capture and sort single cells on the basis of a clinically relevant mixed sample consisting of benign and cancerous breast cells was demonstrated. The platform achieved a target to non-target capture accuracy of over 95%. Due to the high accuracy in addition to factors such as portability and simplicity, the design shows great promise to be used as a point-of-care diagnostic tool in clinical applications.

The following chapter focuses on the label-free detection of captured cells using non-faradaic electrochemical impedance spectroscopy.

Chapter 5

Cell quantification

For an efficient and reliable cell sorting device, it is important that it readily provides information about the number of cells that have been sorted. With this value, the amount of the sample that still needs to be sorted can be approximated. While certain structures, such as Coulter counters, can be used to detect and count single cells, any additional structure included in the overall platform increases system complexity and hence reduces reliability. Since the presented microfluidic platform is based on IDEs, the same electrodes that are used for DEP capture and cell sorting can be used for non-faradaic electrochemical impedance spectroscopy (nF-EIS) measurements. Only a limited number of reports have been published that combine microwells with subsequent impedimetric measurements.[47], [92] The electrode structure of these devices is fundamentally different from our proposed platform as they feature two large electrode planes located at the top and bottom of the channel. Consequently, the sensitivity of the platform discussed in this thesis should be higher, as individual small sectors are equipped with separate IDEs.

5.1 Configuration of platform

5.1.1 Impedimetric quantification of sector occupancy

In order to quantify the correlation between impedance and number of cells occupying a given sector, nF-EIS measurements were taken for different levels of occupancy. First, MCF-10A cells prepared at a concentration of 50 cells/μL were injected at a flow rate of 0.8 μL/min. Meanwhile, a DEP signal of 15 V_{pp}

and 1 MHz was applied to the sector under test. The nanowell occupancy was closely monitored using a fluorescence microscope. Once a certain occupancy level was reached, the DEP signal was turned off and the impedance analyzer connected to the sector. As the flow rate was low, no cells escaped from the nanowells while nF-EIS measurements were conducted for approximately 20 s. Once the impedance frequency response measurement was finished, the DEP signal was turned back on and the process was repeated at higher occupancy levels. Three independent experiments were conducted for each sector. Figure 5.1 shows the typical impedance frequency responses of a sector for different sector occupancies. The IDE array forms a capacitive-based sensor with the frequency response of the overall system impedance $Z_{sys}(\omega)$ given by Equation 2.5. Note that impedance is a complex measure and can be separated into a magnitude response component and a phase response component.

The magnitude response decreased with an increase in frequency (Figure 5.1a). The phase response started at -83 degrees, reached a peak in the resistive region of the spectrum, and tended to -90 degrees after passing the peak (Figure 5.1b). This behaviour can be explained by the fact that the low and high frequency regimes are dominated by C_{dl} and C_{geo}, respectively, thus showing a highly capacitive response. However, at mid-frequencies the impedance response becomes resistive, resulting in an increase in phase as well as in a decrease in the slope of the magnitude response. As seen in Figure 5.1a, a higher level of occupancy resulted in lower magnitude responses. This is due to captured cells increasing the overall system capacitance by introducing a change in conductivity and permittivity. Consequently, a shift of the resistive region of the spectrum towards higher frequencies occurred as the system became more conductive, which could be observed in the phase response. This is in agreement with previously reported results of measured impedance frequency responses for IDE structures.[81]

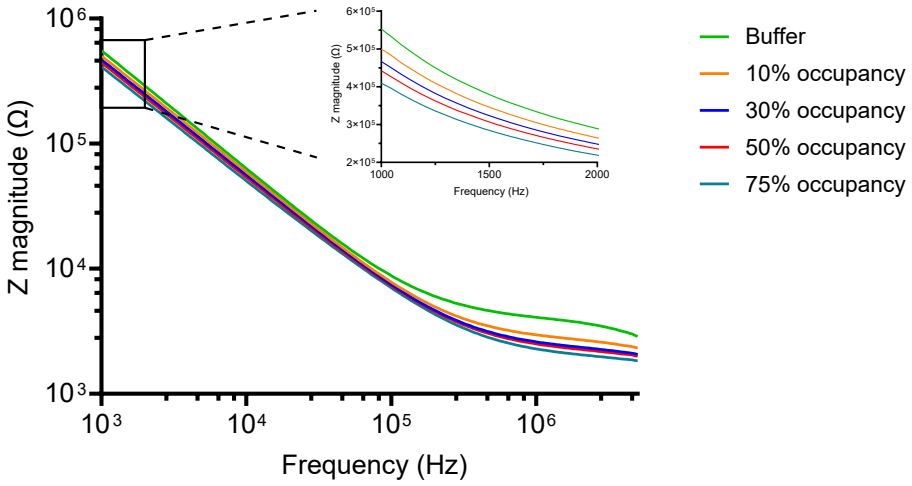

(a)

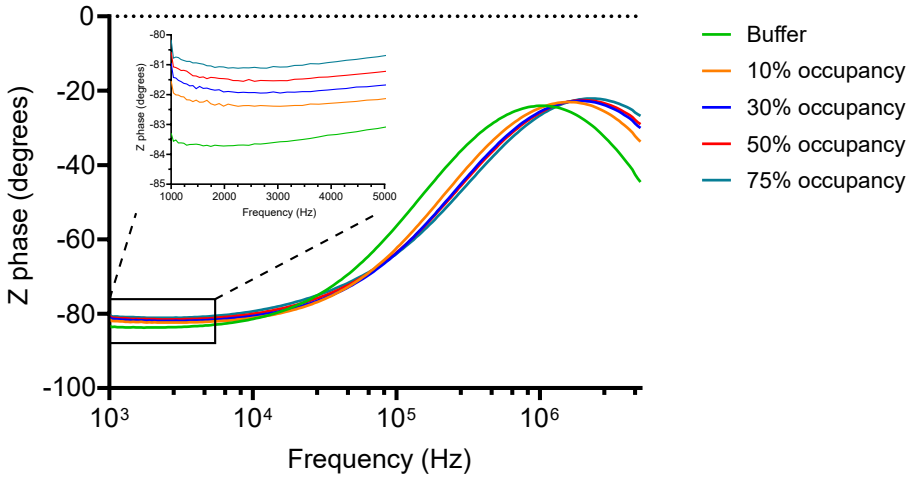

(b)

Figure 5.1: Measured impedance frequency responses obtained for different sector occupancies. Impedance magnitude and impedance phase as a function of frequency for different sector occupancies are shown in Figure 5.1a and 5.1b, respectively.

Since these results clearly show that the number of captured cells modulates the impedance response of the microfluidic platform, calibration curves were taken to quantify the change in impedance and relate it to the respective occupancy. To account for impedance response variations of different sectors, the normalized impedance change, Z_{norm}, was defined as

$$|Z_{norm}| = \left| \frac{Z_{cell} - Z_{buffer}}{Z_{buffer}} \right| \tag{5.1}$$

where Z_{cell} is the impedance response measured at a given cell occupancy, and Z_{buffer} the baseline impedance response of the buffer. Note that Z_{norm} is a dimensionless measure normalized by the buffer impedance. The calibration curves of the normalized impedance magnitude plotted against the number of captured cells for frequencies of 2 kHz, 200 kHz, and 2 MHz are shown in Figure 3c. The experimental data was fitted with a linear regression and yielded an R^2 value of 0.9893 and slope of $0.21 * 10^{-3}$ for 2 kHz. For 200 kHz and 2 MHz, the R^2 values and slopes were 0.9364, and 0.9259 as well as $0.15 * 10^{-3}$ and $0.23 * 10^{-3}$, respectively. The single cell sensitivity of the chip can be expressed by the percentage of impedance change caused by a single cell and can be determined by multiplying the slope by 100. In order to better represent the sensitivity of an entire sector which is unlikely to have captured only a single cell, the impedance change caused by 25 captured cells was calculated from experimental data. This corresponds to the expected number of cells which in the case of single cell capture per nanowell can be found in half of a column of the electrode array, referred to as the half-column c_{half}. Following this definition, the sensitivities were $0.525\%/c_{half}$ for 2 kHz, $0.375\%/c_{half}$ for 200 kHz, and $0.575\%/c_{half}$ for 2 MHz. Taking calibration curves for the normalized phase in the same way gave results with generally lower R^2 values and also less inclined slope (Figure 3d). R^2 values of 0.9952 for 2 kHz, 0.8821 for 200 kHz, and 0.8930 for 2 MHz could be obtained. The decrease in slope led to a lower sensitivity with $0.046\%/c_{half}$ for 2 kHz, $0.311\%/c_{half}$ for 200 kHz, and $0.165\%/c_{half}$ for 2 MHz.

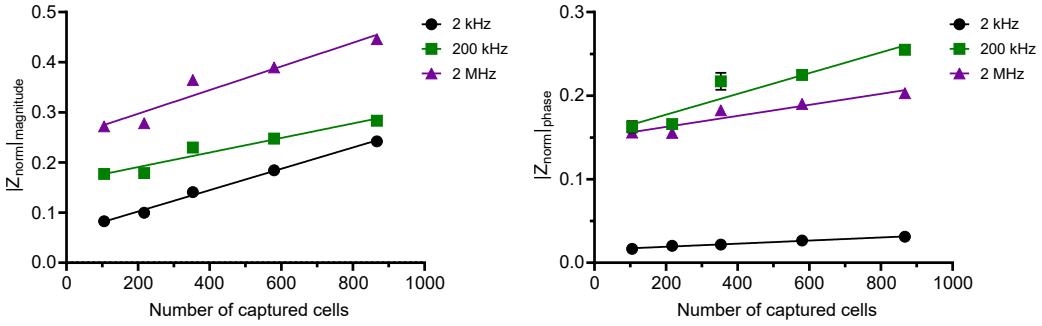

Figure 5.2: Calibration curves of the normalized impedance magnitude and phase taken at frequencies of 2 kHz, 200 kHz, and 2 MHz.

5.1.2 Discussion

The results show that phase measurements are not very sensitive to a change in occupancy and therefore not suitable for dependable monitoring. Magnitude measurements on the other hand show a much higher sensitivity as a significant increase of normalized impedance magnitude can be detected with a rising number of captured cells. The latter can hence be used to reliably monitor and quantify the occupancy of a single or multiple sectors.

To describe the minimum resolution of a sensing system, the limit of detection is normally used. Further measurements would need to be taken at low numbers of of captured cells to accurately determine the limit of detection of the presented platform. However, since the platform is not intended to be used for the capture and detection of only a single or few cells per sector, this parameter is not as critical. Rather, impedimetric measurements should be used to give operators an idea of how much of the sample has been sorted. However, from the results presented in this section it is visible that at 10% occupancy, the lowest measured occupancy, a significant impedance change already occurred. Hence, it is likely that the limit of detection for a sector with 1000 nanowells is quite low.

5.2 Improved chip-holder

The chip-holder presented in Chapter 3 had several practical drawbacks. The two major ones were both related to the electrical connection of external equipment. Firstly, as the same pair of pins had to be used for both DEP capture and subsequent impedance measurements, equipment had to constantly be connected and disconnected. Secondly, since only standard pin headers were used, no cables with good high-frequency properties could be connected.

5.2.1 Design choices and operating principle

To address these drawbacks, a new PCB incorporating various design changes was designed. A block diagram of the modified design is shown in Figure 5.3. To enhance the connections, three BNC connectors were included in the improved chip-holder design. These allowed to easily connect the function generator that applied the DEP signal and the impedance analyzer to the PCB via co-axial cables. Additionally, high-speed RF Reed relays (9002-12-01, Coto Technology) were used to switch between DEP capture and EIS mode. The reed relays were controlled individually by an Arduino Nano (ATmega 328), which allowed to change the active/inactive period of each relay either between or during experiments. An example of signal application to a sector is shown schematically in Figure 5.4. Lastly, the switching matrix responsible for sector selection was updated as well. In the previous version, different signals could only be applied to adjacent sectors, but not to an arbitrary selection. A subsequent trace redesign in combination with new switches allowed signal application to any sector configuration. The schematic for the PCB is included in Appendix C.

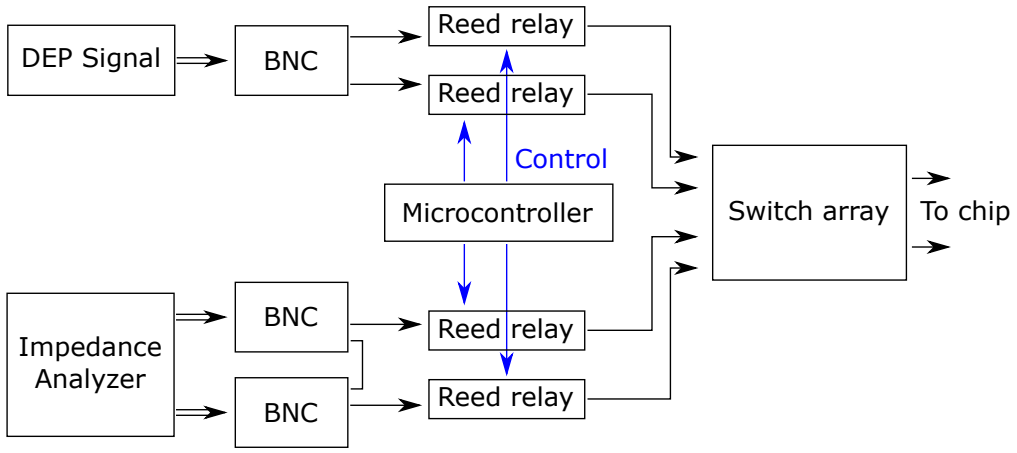

Figure 5.3: Block diagram of the modified chip-holder design. The DEP signal and impedance analyzer are connected via BNC connectors. Two traces of the impedance analyzer are shorted to allow for two-terminal measurements. The microcontroller controls reed relays to switch between DEP capture and EIS measurement mode. The signal which is let through is then applied to the sectors selected in the routing switch array.

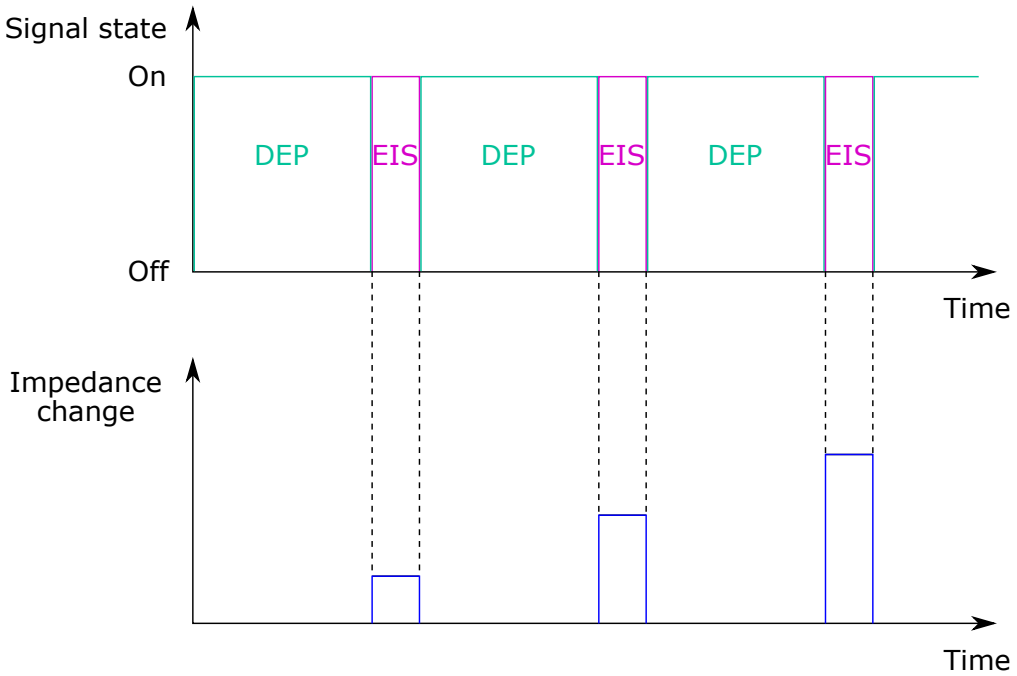

Figure 5.4: Interleaved application of DEP and EIS signals to a sector on the microfluidic platform, controlled by the microcontroller. EIS measurements taken after a longer time show a greater impedance change as more cells are captured in the nanowells.

5.3 Conclusion

This chapter examined whether the IDE structures used for DEP capture and cell sorting can also be used to reliably detect and quantify captured cells using non-faradaic electrochemical impedance spectroscopy. The ability to readily provide information about the amount of sample that is already sorted is important for any cell sorting device. Impedance measurements taken at different sector occupancies and calibration curves calculated from those results were discussed. These showed that the impedance magnitude and phase change is large enough to differentiate different occupancies. The magnitude calibration curve showed a greater increase in value with rising sector occupancy and hence is the preferred indicator. Additionally, a new version of the chip-holder was presented that incorporated a number of quality-of-life updates.

The next chapter explores how the microfluidic platform can be modified to a single-cell RNA sequencing platform as well as looks at which requirements are needed to integrate the platform into a complete point-of-care device.

Chapter 6

Ongoing and future work

While the previous chapters discussed the ideas and results of concluded experiments, this chapter focuses on ongoing and future work, based on the developed microfluidic platform. In the first section the possibility of expanding microfluidic platform into a single-cell RNA sequencing is explored. The second section aims to provide a brief overview of all the components needed for a complete integrated point-of-care device based on the cell sorting platform and how those might look like.

6.1 Expansion to single-cell RNA sequencing platform

Single-cell RNA sequencing (scRNA-Seq) is a technique that allows for the sequencing and subsequent analysis of individual cells and has gained a lot of attention in recent years. scRNA-Seq can provide information, such as uncovering rare cell populations or new relationships between genes, that is hard to obtain with traditional sequencing methods such as bulk sequencing. The main idea of scRNA-Seq is to physically separate cells into individual containment structures, for example well structures, followed by subsequent lysis of the cell. The lysed RNA then has to bind to a particle, most commonly to polystyrene beads coated with barcoded RNA primers, in order to be extracted and analyzed. However, there are still a number of aspects that need to be optimized related to both the engineering side, which include microfluidic fabrication and cell isolation, as well as to the biological and clinical side,

which include library preparation and processing of data.[16], [17], [93]–[96] Since the capabilities of the developed microfluidic platform to selectively sort and capture single cells was successfully verified, modifying its design may offer an integrated solution for both single-cell sorting and capture as well as subsequent single-cell RNA sequencing.

6.1.1 Modified platform design

One of the main criteria when designing nanowell based scRNA-Seq chips is to ensure that only one cell is trapped in each nanowell. As cell size varies within one population, there always is the possibility that two smaller cells will be trapped in the same nanowell, making it difficult to ensure complete single-cell capture. Due to this, the well diameter and height should be around the average cell size, leaving some leeway for fabrication processes. Since the design used for the cell sorting platform was already adjusted to the average sizes of MDA-MB-231 and MFC-10A cells, the same diameter and SU-8 layer height of 20 μm was chosen for the nanowells capturing the cell. While there are many different existing approaches aimed at combining the trapped cells with the primer coated bead, such as dropping them into the same well in DropSeq [93] or sandwich structures that need to be flipped to combine both particles,[17] the here proposed scRNA-Seq design consists out of two adjacent and semi-connected wells, referred to as double-well design.

The nanowell capturing the bead is larger and has a diameter of 35 μm as the barcoded beads had an average diameter of 30 μm.[1] Both nanowells for bead and cell capture intersect with each other, allowing for a small 10 μm side opening between both wells (Figure 6.1). This opening should be small enough to allow lysed cell materials to travel into the well with the bead, but prevent unlysed cells from doing so. Cells are sorted and trapped the same way as described earlier, while polystyrene beads are captured without DEP assistance. Initial experiments using chips only aimed to examine bead capture showed that at a low flow rate, beads are heavy enough to drop into

[1] I would like to thank Lacey Haddon and Dr. Michael Chu for providing the barcoded beads.

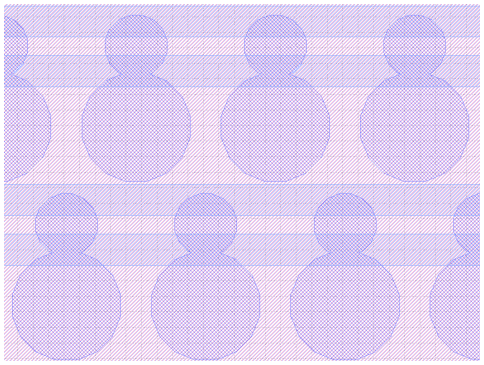

Figure 6.1: Double-well design of scRNA-Seq modification. The upper nanowell captures a single cell and the lower one a barcoded bead. A small opening between both wells allows lysed cell material to travel into the nanowell with the bead.

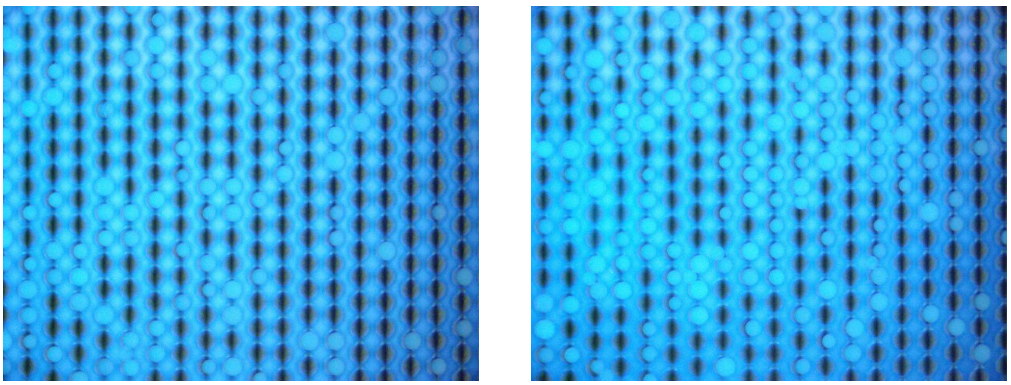

(a) Bead capture after 5 min.

(b) Bead capture after 10 min.

Figure 6.2: Capture of RNA primer coated beads using only gravity at a low flow rate of 5 μL/min and bead concentration of 50 000 beads/ml. The chips used for these initial tests had slightly below 14 000 nanowells with a diameter of 50 μm. Figures 6.2a and 6.2b show how bead capture increases with time.

wells using gravity alone, as shown in Figure 6.2. The photolithography masks for both the scRNA-seq design as well as for the chips used for the initial bead experiments are provided in Appendix B.

6.1.2 Single-cell RNA sequencing process flow

Up to this point, scRNA-Seq results of already concluded experiments have been presented. The microfluidic process flow for the double-well platform as outlined below was created on the basis of results and experiences gained while working with the initial microfluidic platform, but may need to be adjusted

and optimized for efficient scRNA-Seq. Figure 6.3 illustrates the main steps of the process flow.

1. Prime platform.
    - Flow 250 μL ethanol at a flow rate of 10 μL/min.
    - Flow 250 μL DEP buffer to remove remaining ethanol.
2. Use DEP to capture cells suspended in DEP buffer and injected at a flow rate of 0.8 μL/min. The cell concentration should not be too high and preferably at a few hundred cells per μL. The DEP signal parameters depend on cell type.
3. Inject beads at a flow rate of 5 μL/min and concentration that facilitates a good distribution across the chip without any clogging.
4. Cell lysis.
    - Introduce lysis buffer at 5 μL/min and wait until all cells are lysed.
    - Tilt chips slightly to allow lysed material to enter the well with the bead.
5. Flip chips over while maintaining a flow rate of 5 μL/min to extract beads containing the RNA of the lysed cells.

6.2 Integrated point-of-care device

To successfully integrate the microfluidic platform into a complete point-of-care (POC) device, many design choices have to be made. The main focus is creating a device that is both cheap and easy to manufacture as well as reliable and accurate. Additional aspects, such as portability and connectivity to existing infrastructures may be important, depending on the area where the device is intended to be used.

The block diagram shown in Figure 6.4 gives a brief overview of all the components needed for a complete POC device. While the equipment used

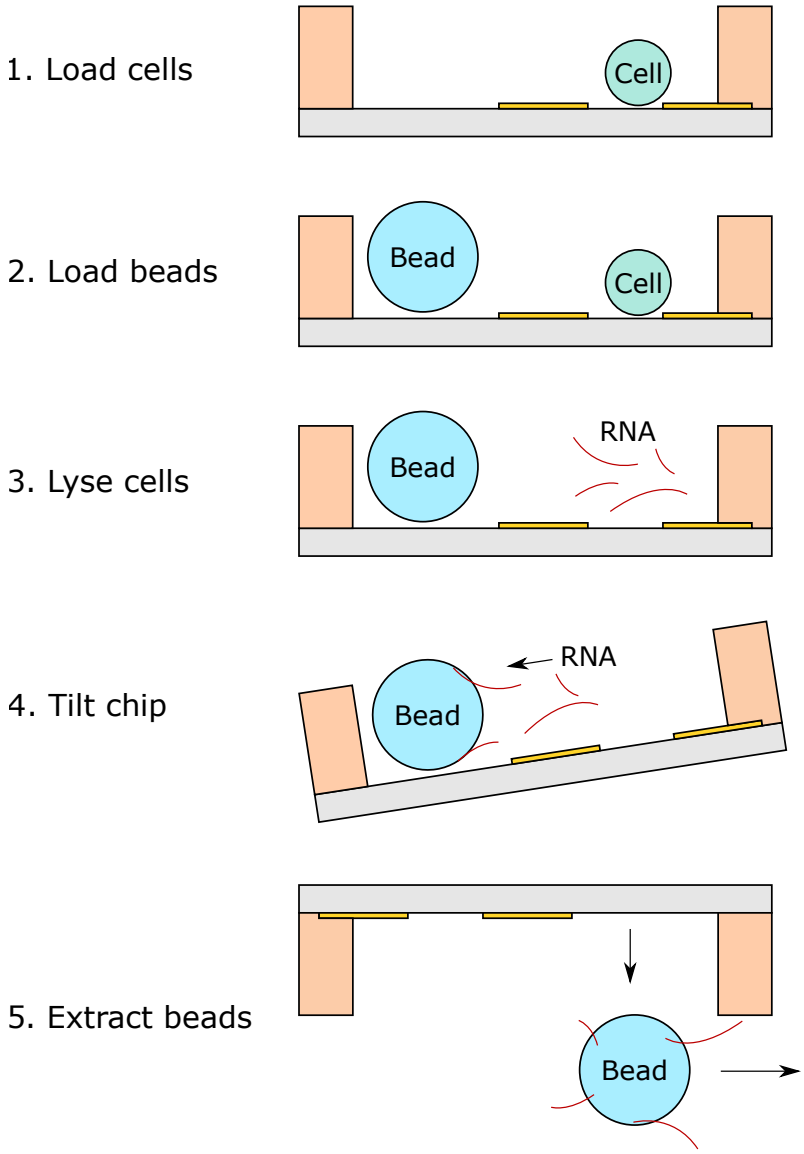

Figure 6.3: Process flow of single-cell RNA sequencing on modified platform (schematic cross-sectional view of a single double-well structure). First, cells and beads are loaded into their respective well. Then cells are lysed and the platform subsequently tilted to allow for RNA to travel to the barcoded bead and bind to it. Finally, the platform is flipped to allow for bead extraction.

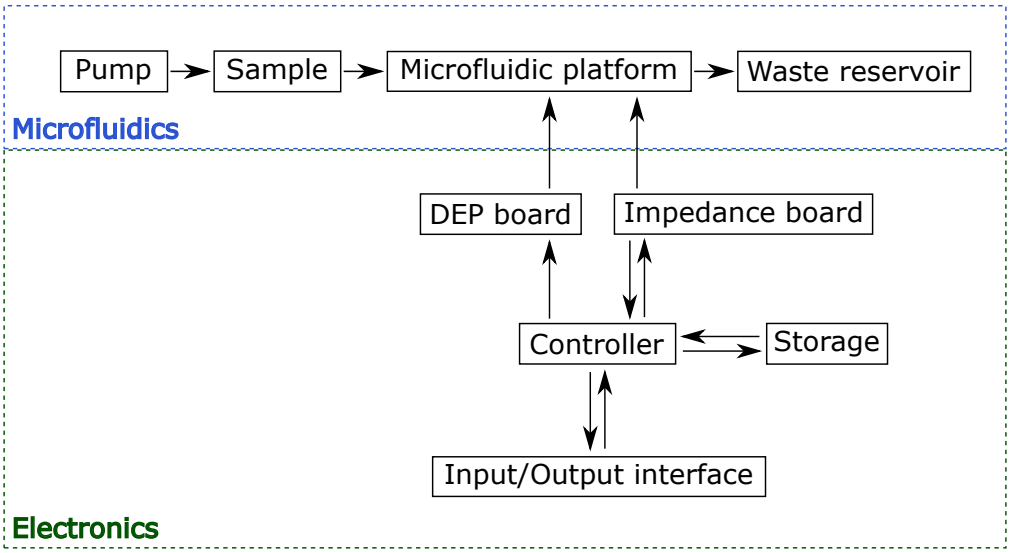

Figure 6.4: Block diagram of integrated point-of-care device. The components can generally be separated into electronics and microfluidics.

to conduct the experiments presented in this thesis was bulky and did cost a significant amount of money, this is not feasible for a POC device. Instead, custom-made designs would have to be made, such as a dedicated DEP and impedance analysis board. The designs can be streamlined to only include the necessary functions rather then offering the flexibility of lab test equipment. Furthermore, the POC device would need to have an integrated controller that handles all necessary tasks, as the patient using the device can not be expected to have sufficient knowledge about the individual processes required for the system to work. On the microfluidic side, attention would have to be given to the type of pump and tubing used, since it should be ensured that there is no cross-contamination between measurements. Alternatively, a cleaning buffer could be flowed throughout the platform during measurements. Finally, the system would have to include enough inputs and outputs for data to be sufficiently saved, monitored, and represented to the patient.

6.3 Conclusion

In this chapter, ongoing work on how the cell sorting platform can be expanded into a single-cell RNA sequencing platform was presented. The main aspects of single-cell sequencing were introduced and preliminary results were discussed. Based on these, a potential process flow that can be used with the expanded chip design was provided. Furthermore, a brief discussion highlighted which components would be needed to integrate the platform into a future point-of-care device.

Chapter 7

Conclusion

Nowadays, the selective sorting of cells is of growing importance in numerous biomedical applications. At the start of the project the goal was clear, to improve and optimize cell sorting platforms currently being used. After studying the existing platforms, it became evident that these were innately limited by their number of output channels, as the number of individually sorted cell types directly corresponds to the number of outlets. Hence, a novel cell sorting platform based on combining nanowells with interdigitated electrodes was developed. Dielectrophoresis was used to selectively sort and capture single cell types without the need for prior labelling. Experimental results obtained with a mixed sample of benign (MCF-10A) and malignant (MDA-MB-231) breast cells showed a target to non-target sorting accuracy of over 95%. Furthermore, as the cell sorting chip was developed as a platform technology rather than as a chip dedicated to only sort specific cell types, it should be easily modifiable to facilitate sorting of numerous different cell types. Therefore, another novelty aspect lies in the versatility of the device.

Another key area of cell sorting that was improved during the course of this project was the use of one electrode structure for both cell sorting and cell detection, decreasing system complexity. Electrochemical impedance spectroscopy was used to readily provide information about the number of captured and hence sorted cells.

Lastly, the design and capture efficiency of the cell sorting platform make it an ideal candidate for potential single-cell RNA sequencing. Current sequenc-

ing approaches do not have the capabilities to selectively sort and sequence cells from a mixed sample, but generally also feature a well structure where sequencing takes place. Hence, the existing platform could be slightly modified to accommodate cell sequencing.

Due to the presented qualities of the platform, such as its high accuracy in addition to its versatility and simplicity, it has the potential to become an essential point-of-care device in areas where sorting of varying cell samples is required.

References

[1] M. J. Tomlinson, S. Tomlinson, X. B. Yang, and J. Kirkham, "Cell separation: Terminology and practical considerations," *Journal of Tissue Engineering*, vol. 4, p. 204 173 141 247 269, 2012. DOI: 10.1177/2041731412472690.

[2] Y. Chen, P. Li, P.-H. Huang, *et al.*, "Rare cell isolation and analysis in microfluidics," *Lab on a Chip*, vol. 14, no. 4, p. 626, 2014. DOI: 10.1039/c3lc90136j.

[3] A. W. Wognum, A. C. Eaves, and T. E. Thomas, "Identification and isolation of hematopoietic stem cells," *Archives of Medical Research*, vol. 34, no. 6, 461–475, 2003. DOI: 10.1016/j.arcmed.2003.09.008.

[4] C. W. S. Iv, C. D. Reyes, and G. P. López, "Microfluidic cell sorting: A review of the advances in the separation of cells from debulking to rare cell isolation," *Lab on a Chip*, vol. 15, no. 5, 1230–1249, 2015. DOI: 10.1039/c4lc01246a.

[5] D. C. Hinshaw and L. A. Shevde, "The tumor microenvironment innately modulates cancer progression," *Cancer Research*, vol. 79, no. 18, 4557–4566, 2019. DOI: 10.1158/0008-5472.can-18-3962.

[6] E. R. Malone, M. Oliva, P. J. B. Sabatini, T. L. Stockley, and L. L. Siu, "Molecular profiling for precision cancer therapies," *Genome Medicine*, vol. 12, no. 1, 2020. DOI: 10.1186/s13073-019-0703-1.

[7] S. Goodwin, J. D. Mcpherson, and W. R. Mccombie, "Coming of age: Ten years of next-generation sequencing technologies," *Nature Reviews Genetics*, vol. 17, no. 6, 333–351, 2016. DOI: 10.1038/nrg.2016.49.

[8] B. E. Slatko, A. F. Gardner, and F. M. Ausubel, "Overview of next-generation sequencing technologies," *Current Protocols in Molecular Biology*, vol. 122, no. 1, 2018. DOI: 10.1002/cpmb.59.

[9] K. C. Andree, G. V. Dalum, and L. W. Terstappen, "Challenges in circulating tumor cell detection by the cellsearch system," *Molecular Oncology*, vol. 10, no. 3, 395–407, 2015. DOI: 10.1016/j.molonc.2015.12.002.

[10] W. J. Allard, J. Matera, M. C. Miller, *et al.*, "Tumor cells circulate in the peripheral blood of all major carcinomas but not in healthy subjects or patients with non-malignant diseases," *Journal of Clinical Oncology*, vol. 22, no. 14, 9552–9552, 2004. DOI: 10.1200/jco.2004.22.90140.9552.

[11] R. S. Hazra, N. Kale, G. Aland, *et al.*, "Cellulose mediated transferrin nanocages for enumeration of circulating tumor cells for head and neck cancer," *Scientific Reports*, vol. 10, no. 1, 2020. DOI: 10.1038/s41598-020-72920-9.

[12] P. Gupta, Z. Gulzar, B. Hsieh, A. Lim, D. Watson, and R. Mei, "Analytical validation of the cellmax platform for early detection of cancer by enumeration of rare circulating tumor cells," *Journal of Circulating Biomarkers*, vol. 8, pp. 1–13, 2019. DOI: 10.1177/1849454419899214.

[13] A. Atkins, P. Gupta, B. M. Zhang, *et al.*, "Detection of circulating tumor dna with a single-molecule sequencing analysis validated for targeted and immunotherapy selection," *Molecular Diagnosis and Therapy*, vol. 23, pp. 521–535, 2019. DOI: 10.1007/s40291-019-00406-0.

[14] D. T. Montoro, A. L. Haber, M. Biton, *et al.*, "A revised airway epithelial hierarchy includes CFTR-expressing ionocytes," *Nature*, vol. 560, no. 7718, 319–324, 2018. DOI: 10.1038/s41586-018-0393-7.

[15] G. X. Y. Zheng, J. M. Terry, P. Belgrader, *et al.*, "Massively parallel digital transcriptional profiling of single cells," *Nature Communications*, vol. 8, 2017. DOI: 10.1038/ncomms14049.

[16] B. Dura, J.-Y. Choi, K. Zhang, *et al.*, "ScFTD-seq: Freeze-thaw lysis based, portable approach toward highly distributed single-cell 3 mRNA profiling," *Nucleic Acids Research*, vol. 47, no. 3, 2018. DOI: 10.1093/nar/gky1173.

[17] Z. Bai, Y. Deng, D. Kim, Z. Chen, Y. Xiao, and R. Fan, "An integrated dielectrophoresis-trapping and nanowell transfer approach to enable double-sub-poisson single-cell RNA sequencing," *ACS Nano*, vol. 14, no. 6, 7412–7424, 2020. DOI: 10.1021/acsnano.0c02953.

[18] A. Morimoto, T. Mogami, M. Watanabe, *et al.*, "High-density dielectrophoretic microwell array for detection, capture, and single-cell analysis of rare tumor cells in peripheral blood," *Plos One*, vol. 10, no. 6, 2015. DOI: 10.1371/journal.pone.0130418.

[19] H. A. Pohl, "The motion and precipitation of suspensoids in divergent electric fields," *Journal of Applied Physics*, vol. 22, no. 7, 869–871, 1951. DOI: 10.1063/1.1700065.

[20] H. A. Pohl and I. Hawk, "Separation of living and dead cells by dielectrophoresis," *Science*, vol. 152, no. 3722, 647–649, 1966. DOI: 10.1126/science.152.3722.647-a.

[21] X. Hu, P. H. Bessette, J. Qian, C. D. Meinhart, P. S. Daugherty, and H. T. Soh, "Marker-specific sorting of rare cells using dielectrophoresis," *Proceedings of the National Academy of Sciences*, vol. 102, no. 44, 15757–15761, 2005. DOI: 10.1073/pnas.0507719102.

[22] R. S. W. Thomas, P. D. Mitchell, R. O. C. Oreffo, H. Morgan, and N. G. Green, "Image-based sorting and negative dielectrophoresis for high purity cell and particle separation," *Electrophoresis*, vol. 40, no. 20, 2718–2727, 2019. DOI: 10.1002/elps.201800489.

[23] S. Fiedler, S. G. Shirley, T. Schnelle, and G. Fuhr, "Dielectrophoretic sorting of particles and cells in a microsystem," *Analytical Chemistry*, vol. 70, no. 9, 1909–1915, 1998. DOI: 10.1021/ac971063b.

[24] A. Isozaki, Y. Nakagawa, M. H. Loo, *et al.*, "Sequentially addressable dielectrophoretic array for high-throughput sorting of large-volume biological compartments," *Science Advances*, vol. 6, no. 22, 2020. DOI: 10.1126/sciadv.aba6712.

[25] H. Song, J. M. Rosano, Y. Wang, *et al.*, "Continuous-flow sorting of stem cells and differentiation products based on dielectrophoresis," *Lab on a Chip*, vol. 15, no. 5, 1320–1328, 2015. DOI: 10.1039/c4lc01253d.

[26] D. Lee, B. Hwang, and B. Kim, "The potential of a dielectrophoresis activated cell sorter (DACS) as a next generation cell sorter," *Micro and Nano Systems Letters*, vol. 4, no. 1, 2016. DOI: 10.1186/s40486-016-0028-4.

[27] P. R. C. Gascoyne, S. Shim, J. Noshari, F. F. Becker, and K. Stemke-Hale, "Correlations between the dielectric properties and exterior morphology of cells revealed by dielectrophoretic field-flow fractionation," *Electrophoresis*, vol. 34, no. 7, 1042–1050, 2013. DOI: 10.1002/elps.201200496.

[28] X.-B. Wang, J. Yang, Y. Huang, J. Vykoukal, F. F. Becker, and P. R. C. Gascoyne, "Cell separation by dielectrophoretic field-flow-fractionation," *Analytical Chemistry*, vol. 72, no. 4, 832–839, 2000. DOI: 10.1021/ac990922o.

[29] Y. Huang, J. Yang, X.-B. Wang, F. F. Becker, and P. R. Gascoyne, "The removal of human breast cancer cells from hematopoietic cd34 stem cells by dielectrophoretic field-flow-fractionation," *Journal of Hematotherapy and Stem Cell Research*, vol. 8, no. 5, 481–490, 1999. DOI: 10.1089/152581699319939.

[30] J. Yang, Y. Huang, X.-B. Wang, F. F. Becker, and P. R. C. Gascoyne, "Cell separation on microfabricated electrodes using dielectrophoretic gravitational field-flow fractionation," *Analytical Chemistry*, vol. 71, no. 5, 911–918, 1999. DOI: 10.1021/ac981250p.

[31] P. A. Duarte, L. Menze, G. N. Abdelrasoul, *et al.*, "Single ascospore detection for the forecasting of sclerotinia stem rot of canola," *Lab on a Chip*, vol. 20, no. 19, 3644–3652, 2020. DOI: 10.1039/d0lc00426j.

[32] D. T. Bacheschi, W. Polsky, Z. Kobos, *et al.*, "Overcoming the sensitivity vs. throughput tradeoff in coulter counters: A novel side counter design," *Biosensors and Bioelectronics*, vol. 168, p. 112 507, 2020. DOI: 10.1016/j.bios.2020.112507.

[33] P. Han, S. Yosinski, Z. A. Kobos, *et al.*, "Continuous label-free electronic discrimination of T cells by activation state," *ACS Nano*, vol. 14, no. 7, 8646–8657, 2020. DOI: 10.1021/acsnano.0c03018.

[34] M. Kobayashi, S. H. Kim, H. Nakamura, S. Kaneda, and T. Fujii, "Cancer cell analyses at the single cell-level using electroactive microwell array device," *Plos One*, vol. 10, no. 11, 2015. DOI: 10.1371/journal.pone.0139980.

[35] S. H. Kim and T. Fujii, "Efficient analysis of a small number of cancer cells at the single-cell level using an electroactive double-well array," *Lab on a Chip*, vol. 16, no. 13, 2440–2449, 2016. DOI: 10.1039/c6lc00241b.

[36] Y. Yang, H. S. Rho, M. Stevens, A. G. J. Tibbe, H. Gardeniers, and L. W. M. M. Terstappen, "Microfluidic device for DNA amplification of single cancer cells isolated from whole blood by self-seeding microwells," *Lab on a Chip*, vol. 15, no. 22, 4331–4337, 2015. DOI: 10.1039/c5lc00816f.

[37] Y. Yoshimura, M. Tomita, F. Mizutani, and T. Yasukawa, "Cell pairing using microwell array electrodes based on dielectrophoresis," *Analytical Chemistry*, vol. 86, no. 14, 6818–6822, 2014. DOI: 10.1021/ac5015996.

[38] C. Wu, R. Chen, Y. Liu, Z. Yu, Y. Jiang, and X. Cheng, "A planar dielectrophoresis-based chip for high-throughput cell pairing," *Lab on a Chip*, vol. 17, no. 23, 4008–4014, 2017. DOI: 10.1039/c7lc01082f.

[39] N. J. Wittenberg, H. Im, T. W. Johnson, *et al.*, "Facile assembly of micro- and nanoarrays for sensing with natural cell membranes," *ACS Nano*, vol. 5, no. 9, 7555–7564, 2011. DOI: 10.1021/nn202554t.

[40] T. Man, X. Zhu, Y. T. Chow, *et al.*, "Intracellular photothermal delivery for suspension cells using sharp nanoscale tips in microwells," *ACS Nano*, vol. 13, no. 9, 10835–10844, 2019. DOI: 10.1021/acsnano.9b06025.

[41] S. Bose, Z. Wan, A. Carr, *et al.*, "Scalable microfluidics for single-cell RNA printing and sequencing," *Genome Biology*, vol. 16, no. 1, 2015. DOI: 10.1186/s13059-015-0684-3.

[42] J. Yuan and P. A. Sims, "An automated microwell platform for large-scale single cell RNA-seq," *Scientific Reports*, vol. 6, no. 1, 2016. DOI: 10.1038/srep33883.

[43] H.-C. Moeller, M. K. Mian, S. Shrivastava, B. G. Chung, and A. Khademhosseini, "A microwell array system for stem cell culture," *Biomaterials*, vol. 29, no. 6, 752–763, 2008. DOI: 10.1016/j.biomaterials.2007.10.030.

[44] D. K. Wood, D. M. Weingeist, S. N. Bhatia, and B. P. Engelward, "Single cell trapping and DNA damage analysis using microwell arrays," *Proceedings of the National Academy of Sciences*, vol. 107, no. 22, 10008–10013, 2010. DOI: 10.1073/pnas.1004056107.

[45] B. Cordovez, D. Psaltis, and D. Erickson, "Trapping and storage of particles in electroactive microwells," *Applied Physics Letters*, vol. 90, no. 2, p. 024 102, 2007. DOI: 10.1063/1.2430775.

[46] S. H. Kim, T. Yamamoto, D. Fourmy, and T. Fujii, "Electroactive microwell arrays for highly efficient single-cell trapping and analysis," *Small*, vol. 7, no. 22, 3239–3247, 2011. DOI: 10.1002/smll.201101028.

[47] A. Mansoorifar, A. Koklu, A. C. Sabuncu, and A. Beskok, "Dielectrophoresis assisted loading and unloading of microwells for impedance spectroscopy," *Electrophoresis*, vol. 38, no. 11, 1466–1474, 2017. DOI: 10.1002/elps.201700020.

[48] H. R. Hulett, W. A. Bonner, J. Barrett, and L. A. Herzenberg, "Cell sorting: Automated separation of mammalian cells as a function of intracellular fluorescence," *Science*, vol. 166, no. 3906, 747–749, 1969. DOI: 10.1126/science.166.3906.747.

[49] J. Voldman, "Electrical forces for microscale cell manipulation," *Annual Review of Biomedical Engineering*, vol. 8, no. 1, 425–454, 2006. DOI: 10.1146/annurev.bioeng.8.061505.095739.

[50] F. Guo, K. Liu, X.-H. Ji, *et al.*, "Valve-based microfluidic device for droplet on-demand operation and static assay," *Applied Physics Letters*, vol. 97, no. 23, p. 233 701, 2010. DOI: 10.1063/1.3521283.

[51] B. Yao, G.-A. Luo, X. Feng, W. Wang, L.-X. Chen, and Y.-M. Wang, "A microfluidic device based on gravity and electric force driving for flow cytometry and fluorescence activated cell sorting," *Lab on a Chip*, vol. 4, no. 6, p. 603, 2004. DOI: 10.1039/b408422e.

[52] M. Ward, P. Turner, M. Dejohn, and G. Kaduchak, "Fundamentals of acoustic cytometry," *Current Protocols in Cytometry*, vol. 49, no. 1, 2009. DOI: 10.1002/0471142956.cy0122s49.

[53] O. Jakobsson, C. Grenvall, M. Nordin, M. Evander, and T. Laurell, "Acoustic actuated fluorescence activated sorting of microparticles," *Lab Chip*, vol. 14, no. 11, 1943–1950, 2014. DOI: 10.1039/c3lc51408k.

[54] L. Johansson, F. Nikolajeff, S. Johansson, and S. Thorslund, "On-chip fluorescence-activated cell sorting by an integrated miniaturized ultrasonic transducer," *Analytical Chemistry*, vol. 81, no. 13, 5188–5196, 2009. DOI: 10.1021/ac802681r.

[55] J. Alexandr and P. Zemánek, "Light at work: The use of optical forces for particle manipulation, sorting, and analysis," *Electrophoresis*, vol. 29, no. 24, 4813–4851, 2008. DOI: 10.1002/elps.200800484.

[56] A. Ashkin, "Acceleration and trapping of particles by radiation pressure," *Physical Review Letters*, vol. 24, no. 4, 156–159, 1970. DOI: 10.1103/physrevlett.24.156.

[57] R. W. Applegate, J. Squier, T. Vestad, J. Oakey, and D. W. M. Marr, "Optical trapping, manipulation, and sorting of cells and colloids in microfluidic systems with diode laser bars," *Optics Express*, vol. 12, no. 19, p. 4390, 2004. DOI: 10.1364/opex.12.004390.

[58] J. H. Kang, S. Krause, H. Tobin, A. Mammoto, M. Kanapathipillai, and D. E. Ingber, "A combined micromagnetic-microfluidic device for rapid capture and culture of rare circulating tumor cells," *Lab on a Chip*, vol. 12, no. 12, p. 2175, 2012. DOI: 10.1039/c2lc40072c.

[59] K. Hoshino, Y.-Y. Huang, N. Lane, *et al.*, "Microchip-based immunomagnetic detection of circulating tumor cells," *Lab on a Chip*, vol. 11, no. 20, p. 3449, 2011. DOI: 10.1039/c1lc20270g.

[60] E. Ozkumur, A. M. Shah, J. C. Ciciliano, *et al.*, "Inertial focusing for tumor antigen-dependent and -independent sorting of rare circulating tumor cells," *Science Translational Medicine*, vol. 5, no. 179, 2013. DOI: 10.1126/scitranslmed.3005616.

[61] H. A. Pohl, "Some effects of nonuniform fields on dielectrics," *Journal of Applied Physics*, vol. 29, no. 8, 1182–1188, 1958. DOI: 10.1063/1.1723398.

[62] Y. Harada and T. Asakura, "Radiation forces on a dielectric sphere in the rayleigh scattering regime," *Optics Communications*, vol. 124, no. 5-6, 529–541, 1996. DOI: 10.1016/0030-4018(95)00753-9.

[63] V. Raicu, G. Raicu, and G. Turcu, "Dielectric properties of yeast cells as simulated by the two-shell model," *Biochimica et Biophysica Acta (BBA) - Bioenergetics*, vol. 1274, no. 3, 143–148, 1996. DOI: 10.1016/0005-2728(96)00024-2.

[64] K. Asami, "Characterization of heterogeneous systems by dielectric spectroscopy," *Progress in Polymer Science*, vol. 27, no. 8, 1617–1659, 2002. DOI: 10.1016/s0079-6700(02)00015-1.

[65] Y. Huang, R. Holzel, R. Pethig, and X.-B. Wang, "Differences in the AC electrodynamics of viable and non-viable yeast cells determined through combined dielectrophoresis and electrorotation studies," *Physics in Medi-cine and Biology*, vol. 37, no. 7, 1499–1517, 1992. DOI: 10.1088/0031-9155/37/7/003.

[66] H. Fricke, "The electric capacity of suspensions with special reference to blood," *Journal of General Physiology*, vol. 9, no. 2, 137–152, 1925. DOI: 10.1085/jgp.9.2.137.

[67] R. Pethig and D. B. Kell, "The passive electrical properties of biological systems: Their significance in physiology, biophysics and biotechnology," *Physics in Medicine and Biology*, vol. 32, no. 8, 933–970, 1987. DOI: 10.1088/0031-9155/32/8/001.

[68] D. Holmes, D. Pettigrew, C. H. Reccius, *et al.*, "Leukocyte analysis and differentiation using high speed microfluidic single cell impedance cytometry," *Lab on a Chip*, vol. 9, no. 20, p. 2881, 2009. DOI: 10.1039/b910053a.

[69] G. Qiao, W. Duan, C. Chatwin, A. Sinclair, and W. Wang, "Electrical properties of breast cancer cells from impedance measurement of cell suspensions," *Journal of Physics: Conference Series*, vol. 224, p. 012 081, 2010. DOI: 10.1088/1742-6596/224/1/012081.

[70] G. Qiao, W. Wang, W. Duan, F. Zheng, A. J. Sinclair, and C. R. Chatwin, "Bioimpedance analysis for the characterization of breast cancer cells in suspension," *IEEE Transactions on Biomedical Engineering*, vol. 59, no. 8, 2321–2329, 2012. DOI: 10.1109/tbme.2012.2202904.

[71] A. Han, L. Yang, and A. B. Frazier, "Quantification of the heterogeneity in breast cancer cell lines using whole-cell impedance spectroscopy," *Clinical Cancer Research*, vol. 13, no. 1, 139–143, 2007. DOI: 10.1158/1078-0432.ccr-06-1346.

[72] R. Soffe, S. Baratchi, S.-Y. Tang, P. Mcintyre, A. Mitchell, and K. Khoshmanesh, "Discontinuous dielectrophoresis - a technique for investigating the response of loosely adherent cells to high shear stress," *Proceedings of the 9th International Joint Conference on Biomedical Engineering Systems and Technologies*, 2016. DOI: 10.5220/0005654700230033.

[73] M. Urdaneta and E. Smela, "Multiple frequency dielectrophoresis," *Electrophoresis*, vol. 28, no. 18, 3145–3155, 2007. DOI: 10.1002/elps.200600786.

[74] D. Grieshaber, R. Mackenzie, J. Vörös, and E. Reimhult, "Electrochemical biosensors - sensor principles and architectures," *Sensors*, vol. 8, no. 3, 1400–1458, 2008. DOI: 10.3390/s8031400.

[75] J. Wang, "Electrochemical biosensors: Towards point-of-care cancer diagnostics," *Biosensors and Bioelectronics*, vol. 21, no. 10, 1887–1892, 2006. DOI: 10.1016/j.bios.2005.10.027.

[76] M. C. Rodriguez, A.-N. Kawde, and J. Wang, "Aptamer biosensor for label-free impedance spectroscopy detection of proteins based on recognition-induced switching of the surface charge," *Chemical Communications*, no. 34, p. 4267, 2005. DOI: 10.1039/b506571b.

[77] Y. Peng, D. Zhang, Y. Li, H. Qi, Q. Gao, and C. Zhang, "Label-free and sensitive faradic impedance aptasensor for the determination of lysozyme based on target-induced aptamer displacement," *Biosensors and Bioelectronics*, vol. 25, no. 1, 94–99, 2009. DOI: 10.1016/j.bios.2009.06.001.

[78] G. N. Abdelrasoul, A. Anwar, S. Mackay, *et al.*, "DNA aptamer-based non-faradaic impedance biosensor for detecting e. coli," *Analytica Chimica Acta*, vol. 1107, 135–144, 2020. DOI: 10.1016/j.aca.2020.02.004.

[79] A. S. Tanak, B. Jagannath, Y. Tamrakar, S. Muthukumar, and S. Prasad, "Non-faradaic electrochemical impedimetric profiling of procalcitonin and c-reactive protein as a dual marker biosensor for early sepsis detection," *Analytica Chimica Acta: X*, vol. 3, p. 100 029, 2019. DOI: 10.1016/j.acax.2019.100029.

[80] P. Dak, A. Ebrahimi, and M. A. Alam, "Non-faradaic impedance characterization of an evaporating droplet for microfluidic and biosensing applications," *Lab on a Chip*, vol. 15, no. 3, 931–931, 2015. DOI: 10.1039/c4lc90123a.

[81] S. Rana, R. H. Page, and C. J. Mcneil, "Impedance spectra analysis to characterize interdigitated electrodes as electrochemical sensors," *Electrochimica Acta*, vol. 56, no. 24, 8559–8563, 2011. DOI: 10.1016/j.electacta.2011.07.055.

[82] D. Xu, D. Xu, X. Yu, Z. Liu, W. He, and Z. Ma, "Label-free electrochemical detection for aptamer-based array electrodes," *Analytical Chemistry*, vol. 77, no. 16, 5107–5113, 2005. DOI: 10.1021/ac050192m.

[83] C.-H. Yeh, W.-T. Wang, P.-L. Shen, and Y.-C. Lin, "A developed competitive immunoassay based on impedance measurements for methamphetamine detection," *Microfluidics and Nanofluidics*, vol. 13, no. 2, 319–329, 2012. DOI: 10.1007/s10404-012-0964-0.

[84] K. Aran, L. A. Sasso, N. Kamdar, and J. D. Zahn, "Irreversible, direct bonding of nanoporous polymer membranes to PDMS or glass microdevices," *Lab on a Chip*, vol. 10, no. 5, p. 548, 2010. DOI: 10.1039/b924816a.

[85] Y. Ren, S.-H. Huang, S. Mosser, *et al.*, "A simple and reliable PDMS and SU-8 irreversible bonding method and its application on a microfluidic-mea device for neuroscience research," *Micromachines*, vol. 6, no. 12, 1923–1934, 2015. DOI: 10.3390/mi6121465.

[86] Z. Zhu, P. Chen, K. Liu, and C. Escobedo, "A versatile bonding method for PDMS and SU-8 and its application towards a multifunctional microfluidic device," *Micromachines*, vol. 7, no. 12, p. 230, 2016. DOI: 10.3390/mi7120230.

[87] J. J. Sherba, S. Hogquist, H. Lin, J. W. Shan, D. I. Shreiber, and J. D. Zahn, "The effects of electroporation buffer composition on cell viability and electro-transfection efficiency," *Scientific Reports*, vol. 10, no. 1, 2020. DOI: 10.1038/s41598-020-59790-x.

[88] X. Ren, P. Ghassemi, H. Babahosseini, J. S. Strobl, and M. Agah, "Single-cell mechanical characteristics analyzed by multiconstriction microfluidic channels," *ACS Sensors*, vol. 2, no. 2, 290–299, 2017. DOI: 10.1021/acssensors.6b00823.

[89] T. N. Truongvo, R. M. Kennedy, H Chen, *et al.*, "Microfluidic channel for characterizing normal and breast cancer cells," *Journal of Micromechanics and Microengineering*, vol. 27, no. 3, p. 035 017, 2017. DOI: 10.1088/1361-6439/aa5bbb.

[90] I. Turcan and M. A. Olariu, "Dielectrophoretic manipulation of cancer cells and their electrical characterization," *ACS Combinatorial Science*, vol. 22, no. 11, 554–578, 2020. DOI: 10.1021/acscombsci.0c00109.

[91] E. Salimi, K. Braasch, M. Butler, D. J. Thomson, and G. E. Bridges, "Dielectric model for chinese hamster ovary cells obtained by dielectrophoresis cytometry," *Biomicrofluidics*, vol. 10, no. 1, p. 014 111, 2016. DOI: 10.1063/1.4940432.

[92] A. Mansoorifar, A. Koklu, and A. Beskok, "Quantification of cell death using an impedance-based microfluidic device," *Analytical Chemistry*, vol. 91, no. 6, 4140–4148, 2019. DOI: 10.1021/acs.analchem.8b05890.

[93] E. Z. Macosko, A. Basu, R. Satija, *et al.*, "Highly parallel genome-wide expression profiling of individual cells using nanoliter droplets," *Cell*, vol. 161, no. 5, 1202–1214, 2015. DOI: 10.1016/j.cell.2015.05.002.

[94] B. Hwang, J. H. Lee, and D. Bang, "Single-cell RNA sequencing technologies and bioinformatics pipelines," *Experimental and Molecular Medicine*, vol. 50, no. 8, 1–14, 2018. DOI: 10.1038/s12276-018-0071-8.

[95] A. Haque, J. Engel, S. A. Teichmann, and T. Lönnberg, "A practical guide to single-cell RNA-sequencing for biomedical research and clinical applications," *Genome Medicine*, vol. 9, no. 1, 2017. DOI: 10.1186/s13073-017-0467-4.

[96] G. Chen, B. Ning, and T. Shi, "Single-cell RNA-seq technologies and related computational data analysis," *Frontiers in Genetics*, vol. 10, 2019. DOI: 10.3389/fgene.2019.00317.

Appendix A

Particle parameters

Parameter	Polystyrene bead
$\varepsilon_{r,bead}$	2.6
σ_{bead} (S/m)	$5 * 10^{-4}$
r_{bead} (μm)	8

Table A.1: Detailed parameters of polystyrene bead.

Parameter	HEK-293T	MDA-MB-231	MCF-10A
$\varepsilon_{r,cytoplasm}$	60	60	60
$\sigma_{cytoplasm}$ (S/m)	0.5	1.17	1.40
$\varepsilon_{r,membrane}$	9.5	6.13	13.36
$\sigma_{membrane}$ (S/m)	$7 * 10^{-14}$	$1 * 10^{-6}$	$1 * 10^{-6}$
$r_{cytoplasm}$ (μm)	12.5	7	8.5
$t_{membrane}$ (nm)	7	5	5

Table A.2: Detailed parameters of HEK-293T, MDA-MB-231, and MCF-10A cells.

Parameter	Yeast
$\varepsilon_{r,cytoplasm}$	50
$\sigma_{cytoplasm}$ (S/m)	0.2
$\varepsilon_{r,membrane}$	6
$\sigma_{membrane}$ (S/m)	$25 * 10^{-8}$
$\varepsilon_{r,wall}$	60
σ_{wall} (S/m)	$14 * 10^{-3}$
$r_{cytoplasm}$ (μm)	8
$t_{membrane}$ (nm)	8
t_{wall} (nm)	220

Table A.3: Detailed parameters of yeast cell.

Appendix B

Mask designs

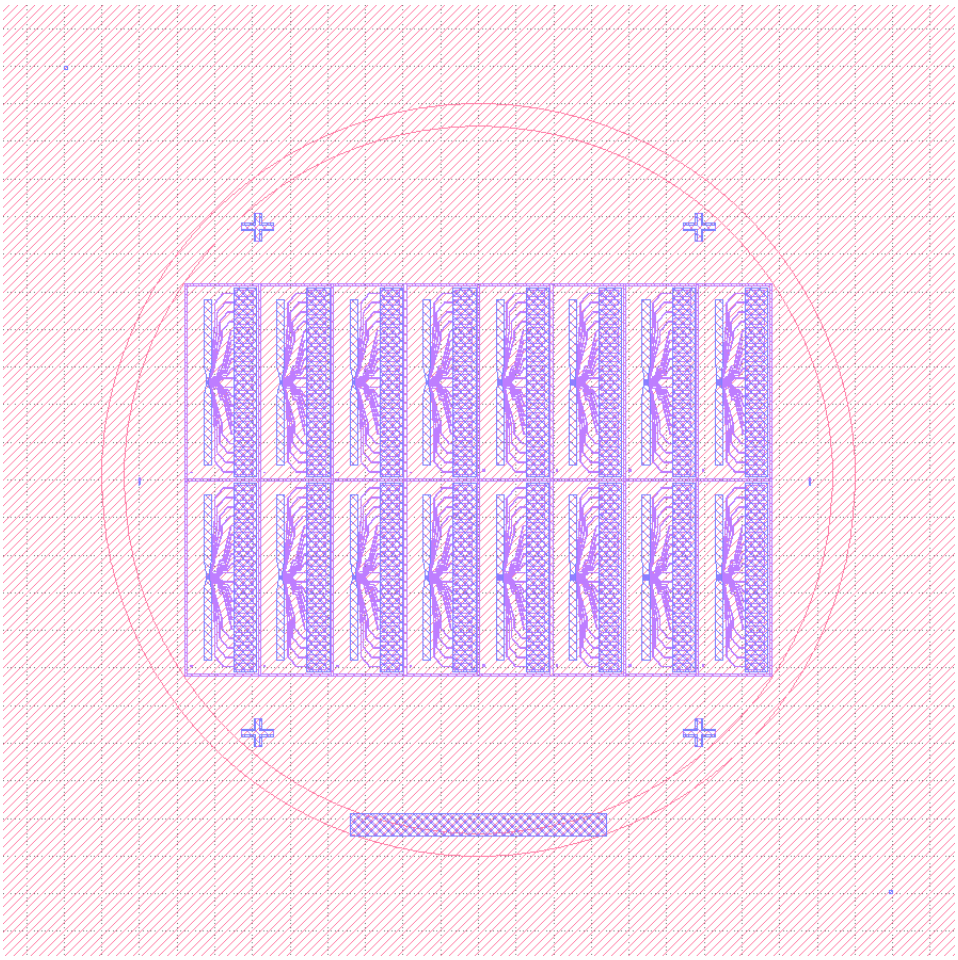

Figure B.1: Mask design used for proof-of-concept experiments. Each chip had 100 nanowells with varying diameters of 10 μm, 15 μm, 20 μm, and 25 μm. 10 nanowells were deposited on each pair of electrodes.

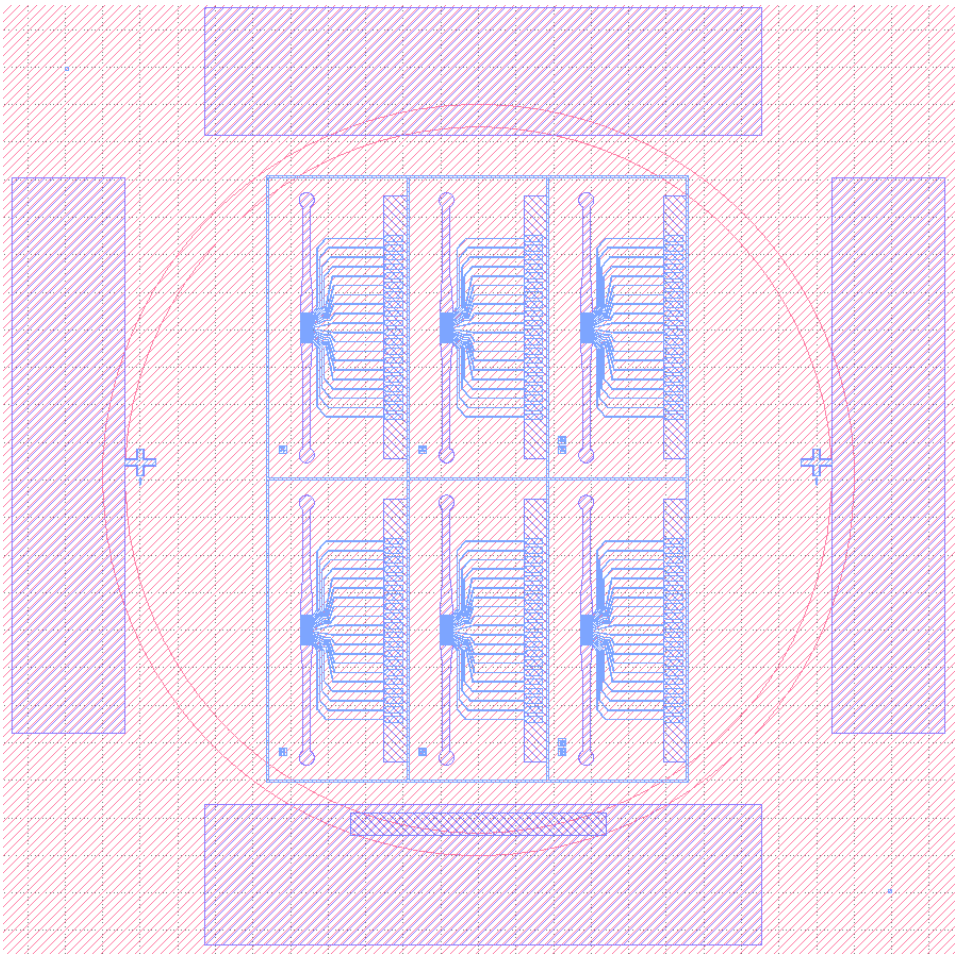

Figure B.2: Mask design of the microfluidic platform. The platform is discussed in-depth in Chapter 4.

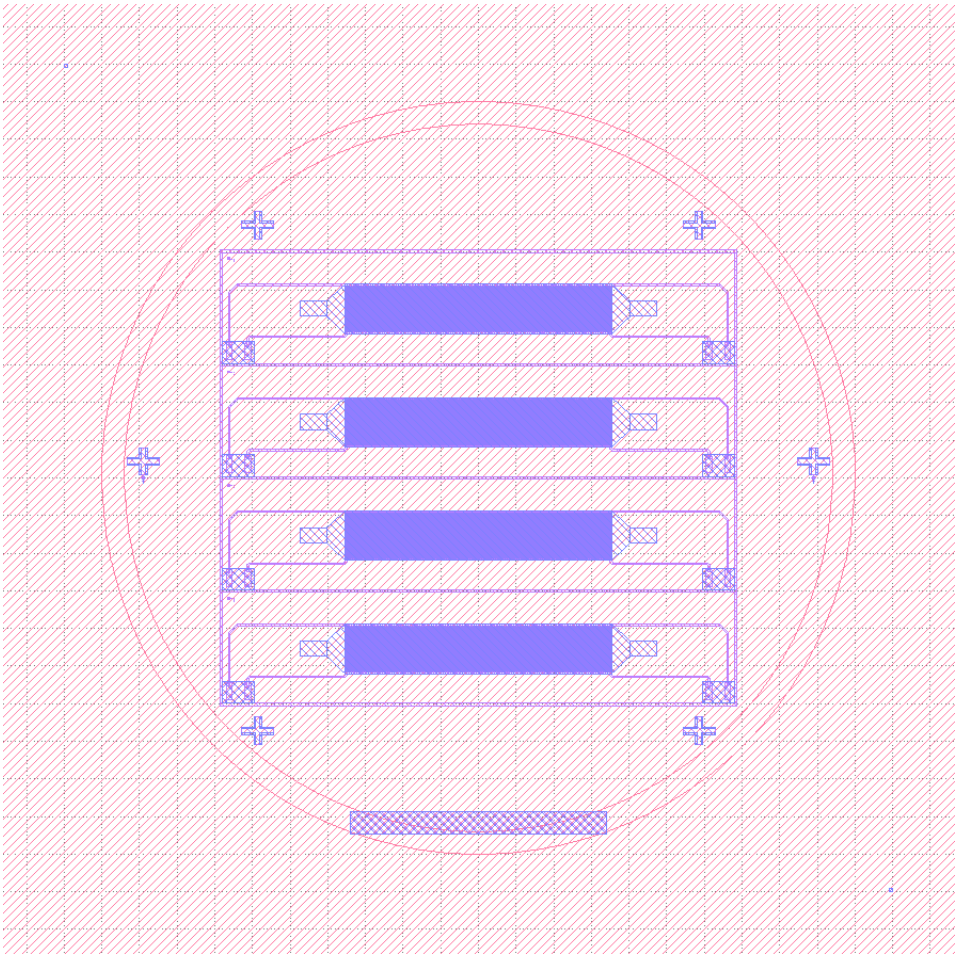

Figure B.3: Mask design used to study RNA coated polystyrene beads. Each chip had slightly less than 14 000 nanowells with a diameter of 50 μm. Electrodes were fabricated at the bottom of the nanowells, although they were not used as bead capture worked well using only gravity for bead loading.

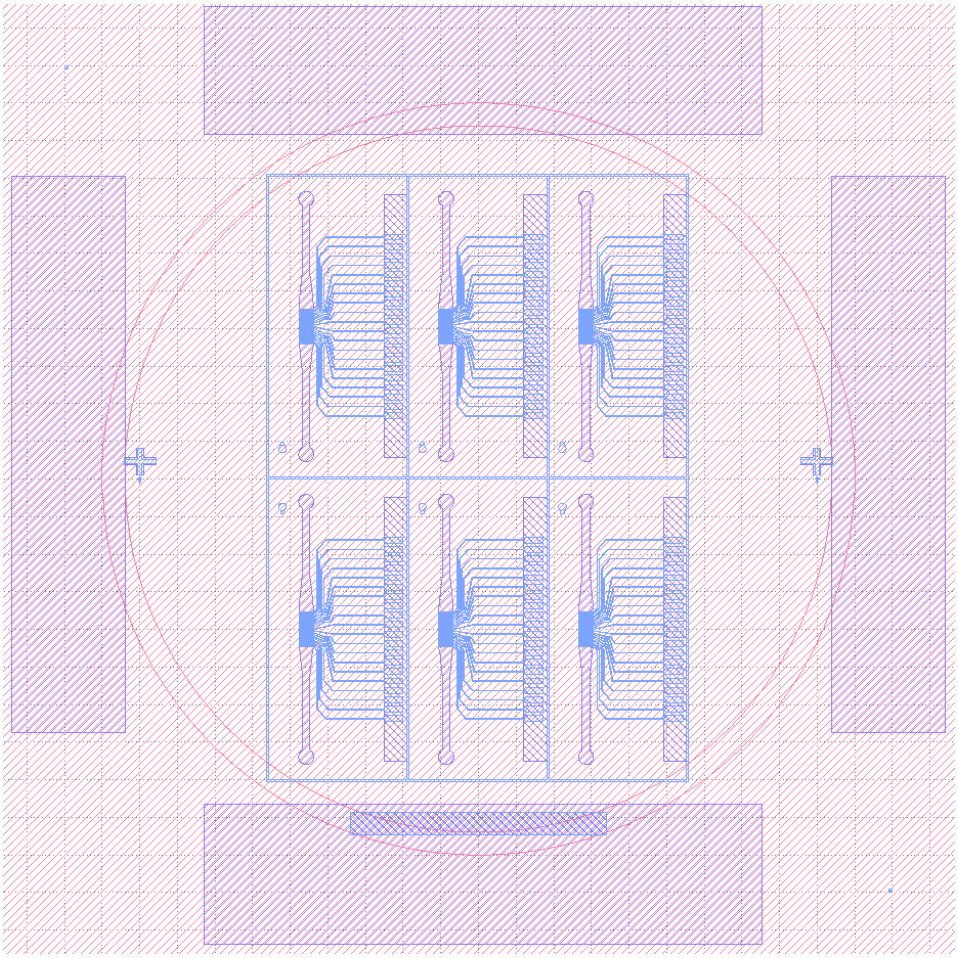

Figure B.4: Mask design used for single-cell RNA sequencing. The double-well design is explained in Chapter 6 and features two nanowells connected by a 10 μm wide opening, allowing for lysed cell contents to pass between wells.

Appendix C

PCB design

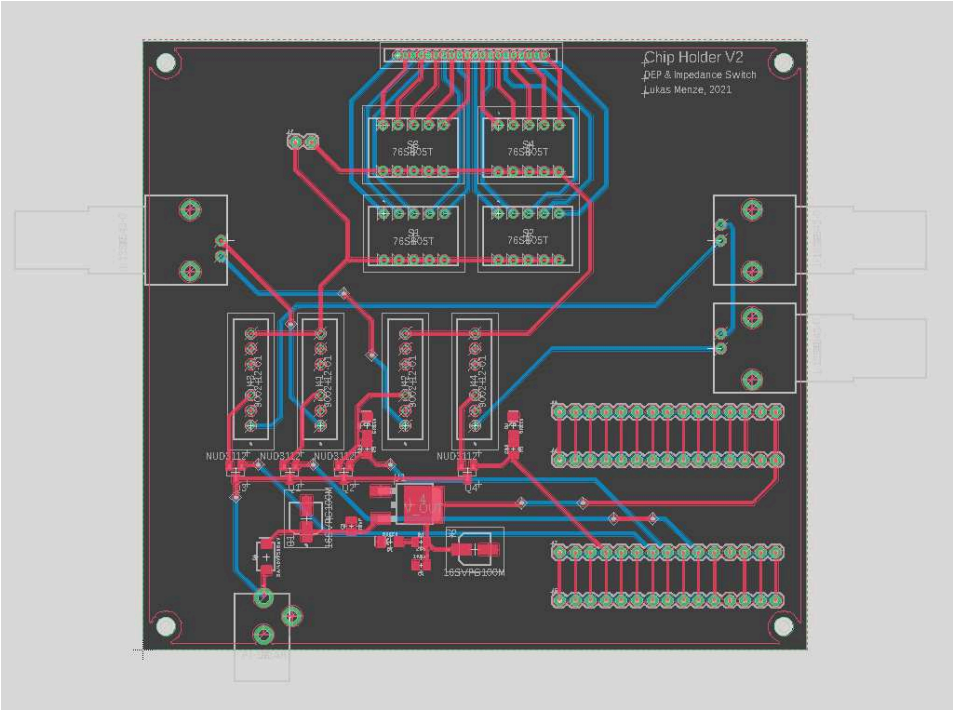

Figure C.1: PCB layout of modified chip-holder.

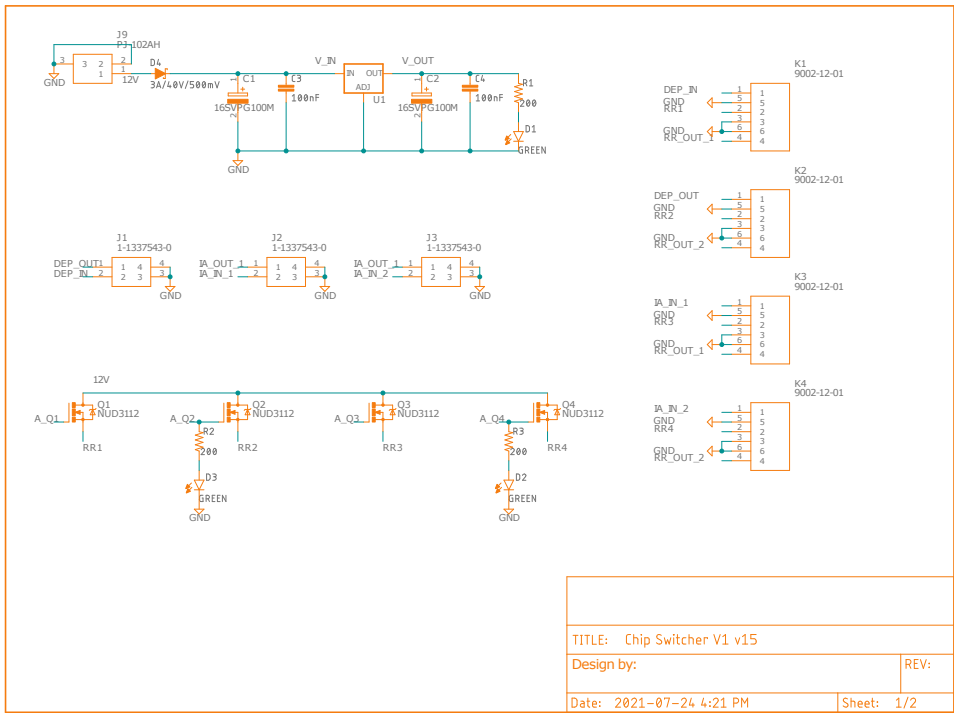

(a)

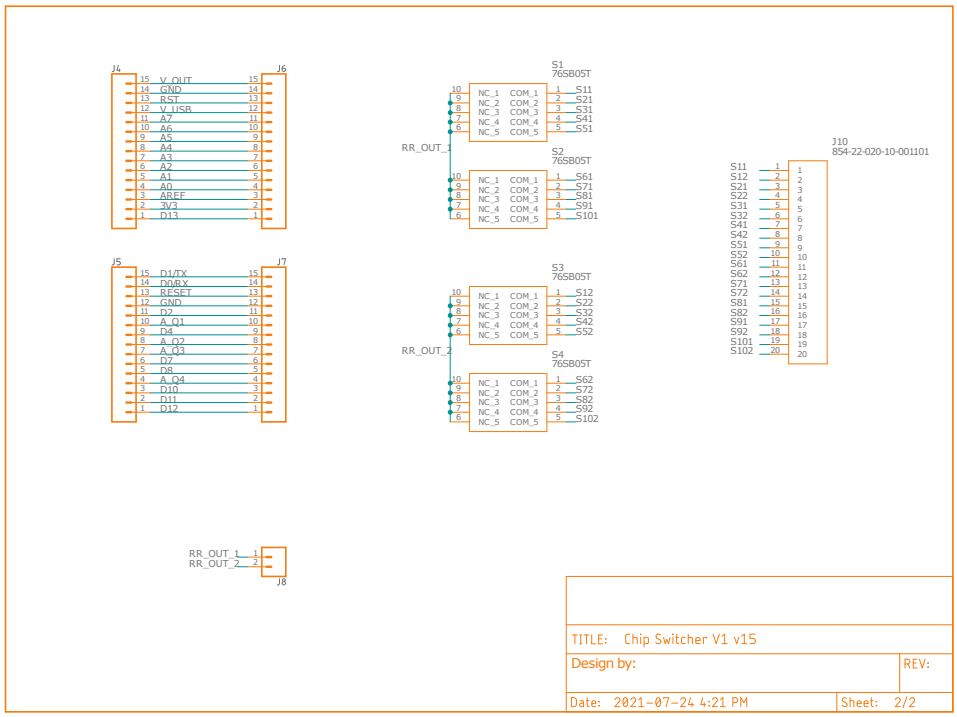

(b)

Figure C.2: PCB schematic of modified chip-holder.